

This is the Post-print version of the following article: *Siegfried Siesgesmund, Rubén López-Doncel, Pascal Sieck, Hendrik Wilke, Klaus Wemmer, Dirk Frei, Sebastián Oriolo, Geochronological and geochemical constraints on the genesis of Cu-Au skarn deposits of the Santa María de la Paz district (Sierra del Fraile, Mexico), Ore Geology Reviews, Volume 94, 2018, Pages 310-325, which has been published in final form at: [10.1016/j.oregeorev.2018.02.010](https://doi.org/10.1016/j.oregeorev.2018.02.010)*

© 2018. This manuscript version is made available under the Creative Commons Attribution-NonCommercial-NoDerivatives 4.0 International (CC BY-NC-ND 4.0) license <http://creativecommons.org/licenses/by-nc-nd/4.0/>

Accepted Manuscript

Geochronological and geochemical constraints on the genesis of Cu-Au skarn deposits of the Santa María de la Paz district (Sierra del Fraile, Mexico)

Siegfried Siesgesmund, Rubén López-Doncel, Pascal Sieck, Hendrik Wilke, Klaus Wemmer, Dirk Frei, Sebastián Oriolo

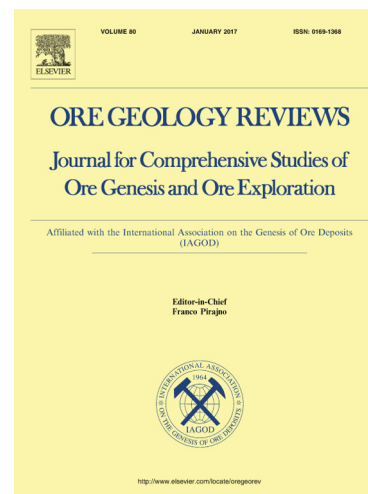
PII: S0169-1368(17)30643-1
DOI: <https://doi.org/10.1016/j.oregeorev.2018.02.010>
Reference: OREGEO 2489

To appear in: *Ore Geology Reviews*

Received Date: 21 August 2017
Revised Date: 22 December 2017
Accepted Date: 6 February 2018

Please cite this article as: S. Siesgesmund, R. López-Doncel, P. Sieck, H. Wilke, K. Wemmer, D. Frei, S. Oriolo, Geochronological and geochemical constraints on the genesis of Cu-Au skarn deposits of the Santa María de la Paz district (Sierra del Fraile, Mexico), *Ore Geology Reviews* (2018), doi: <https://doi.org/10.1016/j.oregeorev.2018.02.010>

This is a PDF file of an unedited manuscript that has been accepted for publication. As a service to our customers we are providing this early version of the manuscript. The manuscript will undergo copyediting, typesetting, and review of the resulting proof before it is published in its final form. Please note that during the production process errors may be discovered which could affect the content, and all legal disclaimers that apply to the journal pertain.



Geochronological and geochemical constraints on the genesis of Cu-Au skarn deposits of the Santa María de la Paz district (Sierra del Fraile, Mexico)

Siegfried Siesgesmund¹, Rubén López-Doncel², Pascal Sieck^{1,3}, Hendrik Wilke¹, Klaus Wemmer¹, Dirk Frei^{4,5}, Sebastián Oriolo^{6*}

¹ Geoscience Centre, Georg-August-Universität Göttingen, Goldschmidtstraße 3, 37077 Göttingen, Germany

² Instituto de Geología, Universidad Autónoma de San Luis Potosí, Av. Manuel Nava 5, 78240 San Luis Potosí, Mexico

³ División de Geociencias Aplicadas, Instituto Potosino de Investigación Científica y Tecnológica (IPICYT), Camino a la Presa San José 2055, Lomas 4° Sección, 78216 San Luis Potosí, Mexico

⁴ Department of Earth Sciences, University of the Western Cape, Private Bag X17, 7530 Bellville, South Africa

⁵ Department of Earth Sciences, Stellenbosch University, Private Bag X1, 7602 Matieland, South Africa

⁶ CONICET-Universidad de Buenos Aires. Instituto de Geociencias Básicas, Aplicadas y Ambientales de Buenos Aires (IGEBA), Intendente Güiraldes 2160, C1428EHA Buenos Aires, Argentina

*Corresponding author: Sebastián Oriolo, seba.oriolo@gmail.com

Abstract

Cu-Au skarn deposits of the mining district of Santa María de La Paz are located in the Sierra del Fraile, in the northern part of San Luis Potosí, Mexico. Samples of four different intrusions and their related skarn deposits were taken underground, in order to obtain whole-rock and mineral geochemical data. U-Pb LA-ICP-MS zircon data indicate crystallization ages of ca. 37.6-35.0 Ma for skarn-related granitic and granodioritic stocks, which show dominant metaluminous to slightly peraluminous, high-K calc-alkaline compositions. These intrusions were emplaced in a post-Laramide continental arc setting under shallow conditions, as suggested by fast cooling inferred

from K-Ar biotite ages of ca. 35-33 Ma. Skarn deposits were contemporaneous with emplacement and crystallization of stocks, as revealed by Re-Os molybdenite geochronological data of exoskarn rocks. Skarn rocks show a general depletion of LILE and REE and a slightly enrichment in HFSE in comparison with intrusive rocks. Pyroxene and garnet show dominant hedenbergite and andradite compositions, respectively. The association of hedenbergite, pyrite, chalcopyrite, native bismuth and pyrrhotite during skarn mineralization suggest reducing conditions, typical for Au but not for Cu skarns. Highest metal contents are concentrated in exoskarn rocks, including anomalies of Cu, Fe, Ni, Sn, Sb, Zn, W and Bi. Metal contents, ore minerals and environmental conditions of skarn rocks, together with whole-rock geochemical data of stocks and pyroxene-garnet compositions, reveal some singularities for the Sierra del Fraile deposits, as they exhibit characteristics of both Cu and Au skarn deposits but might be also compatible with Fe, W, and Zn skarns. Hence, skarn and associated vein deposits of the Sierra del Fraile might have a high potential not only for Cu-Au, but also for several base metals, as reported for comparable post-Laramide skarn and hydrothermal deposits of central and northern Mexico.

Keywords: Cu-Au mineralization, ore deposits, Eocene, post-Laramide magmatism, Re-Os geochronology, andradite-hedenbergite skarn

1. Introduction

Skarns deposits exist in all continents and have been mined for decades because of their large contents of metals. The classification of major skarn deposits is based on their dominant elements, namely Fe, Au, Cu, Zn, W, Mo and Sn (Zharikov, 1970; Einaudi, 1981; Meinert, 1992, Meinert et al., 2005). As most economic skarn deposits are related to magmatic intrusions, the understanding of petrogenesis and tectonic setting of igneous rocks is essential for exploration and classification (Meinert, 1992; Meinert et al., 2005). Additionally, the mineralogical and geochemical data are fundamental for skarn characterization (Einaudi and Burt, 1982; Zharikov et al., 1998; Meinert, 1992), whereas geochronological constraints on both intrusive and associated skarn rocks are critical to assess the timing and duration of ore-forming processes (e.g., Meinert et al., 2005; Chelle-Michou et al., 2015).

Most Mexican Cu and Au deposits are located in western Mexico and comprise a large variety of porphyry-type, skarn, and orogenic deposits, among others, associated with the ca. 80-40 Ma Laramide orogeny (Barton et al., 1995; Albinson and Nelson, 2001; Valencia-Moreno et al., 2006, 2017; Amato et al., 2017; Izaguirre et al., 2017). This orogeny was the result of flat-slab subduction of the Farallón plate beneath the North American plate, and was succeeded by Eocene post-orogenic extension (Dickinson and Snyder, 1978; Clark et al., 1982; Meschede et al., 1997; Bunge and Grand, 2000; Mascuñano et al., 2013; Amato et al., 2017).

The mining district of Santa María de La Paz is located in the Sierra del Fraile, east of Matehuala, in the state of San Luis Potosí, Mexico. This district has been in continuous production for around 150 years and comprises four intrusions and related Cu-(Au) skarn deposits and Ag-Pb-Zn hydrothermal veins, with average grades of 1.3 g/t Au, 150 g/t Ag, 0.9% Cu, 1.8% Zn and 1.1% Pb (Gunnesch et al., 1994; Pinto-Linares, 2008). Pinto-Linares et al. (2008) constrained the age of intrusions at ca. 37-35 Ma, indicating a transitional adakite-like to calc-alkaline geochemical signature.

This work presents new petrographic, mineral and whole-rock geochemical, and geochronological data of intrusions and associated skarns of the Santa María de la Paz mining district, in order to evaluate the petrogenesis of intrusive rocks of the Sierra del Fraile and to characterize skarn deposits and associated ore-forming processes. Further constraints provided by U-Pb LA-ICP-MS zircon ages of intrusive and endoskarn rocks, K-Ar biotite ages of intrusions, and Re-Os molybdenite ages of exoskarns are provided, in order to determine the timing and temporal evolution of intrusions and skarn ore mineralizations.

2. Geological setting

2.1. Regional Geology

The mining district Santa María de la Paz is located at the boundary between two Mesozoic basins, namely the Central Mexico Mesozoic Basin (CMMB) to the west and the Valles-San Luis Potosí Platform (VSLPP) to the east (Fig. 1). The CMMB is constituted by a marine Mesozoic sedimentary sequence of more than 5000 m thickness, with sedimentation beginning in the late Triassic and culminating in the late Cretaceous (Carrillo-Bravo, 1982). The VSLPP consists of Precambrian and Paleozoic metasedimentary rocks, unconformably overlain by Jurassic clastic sediments (Barboza-

Gudiño et al., 2008). Overlaying Precambrian and Jurassic rocks, a Cretaceous marine sequence of evaporites and shallow water limestones occurs, recording a maximum transgression during the Albian-Cenomanian (Carrillo-Bravo, 1982).

The oldest record near the study area are Triassic low-grade metamorphic marine sedimentary rocks (Barboza-Gudiño et al., 1998, 2010; Hoppe et al., 2002), which are unconformably overlain by Lower to Middle Jurassic continental arc deposits of the Nazas Formation or “Nazas Arc” (Pantoja-Alor, 1972; Blickwede, 1981; López-Infanzón, 1986; Barboza-Gudiño et al., 1999, 2008; Bartolini et al., 2003). Marine sedimentation throughout the Mesa Central is recorded from the Oxfordian to the end of Cretaceous. Contemporaneously, more than 4000 m thick, shallow marine carbonate sequences and clastic sediments were accumulated in the VSLPP and CMMB (Carrillo-Bravo, 1982), covering a large portion of the central-eastern Mesa Central between the Late Triassic to Late Cretaceous. Additionally, debris flow and turbiditic deposits are recorded between the western margin of the VSLPP and the transition towards the CMMB (Tamabra Formation; López-Doncel, 2003). All these Mesozoic sequences were strongly deformed during the Laramide orogeny, close to the K/T boundary (Guzmán and de Cserna, 1963; Eguluz-de Antuñano et al., 2000; Tristán-González et al., 2009). Unconformably, a Paleocene-Eocene sedimentary sequence consisting mostly of red beds or of continental clastic deposits overlays Mesozoic rocks, including intercalations of andesitic lavas (49-44 Ma; Aranda-Gómez and McDowell, 1998; Tristán-González et al., 2009) and covering the VSLPP and CMMB. Bimodal volcanism is recorded afterwards, from the early Oligocene until the early Pliocene.

2.2. Study area

The upper Albian to Cenomanian Cuesta del Cura Formation comprises the oldest exposed unit in the study area, consisting of gray, often laminated limestones interbedded with shales (Fig. 1). The thickness of the Cuesta del Cura Formation ranges between 50 m up to 150 m (Barboza-Gudiño et al., 2004). The Cuesta del Cura Formation is overlapped by the Agua Nueva Formation, which consists of limestones, calcareous marls and siltstones of Turonian age (Barboza-Gudiño et al., 2004), and is stratigraphically overlain by the San Felipe and Méndez formations. The latter two comprise siliciclastic rocks, mainly with micro-clasts of volcanic rocks (Nieto-Samaniego et al., 2007). In the region of La Paz, the maximum thickness of both formations is about 100 meters.

Mesozoic sequences are intruded by four granitic stocks (Membrillo, Santa Teresa, Dolores and Cobriza), resulting in contact metamorphic transformations to skarn or hornfels (Fig. 1). Intrusions yielded discordant U-Pb LA-ICP-MS zircon ages of ca. 37-35 Ma and exhibit a transitional adakite-like to calc-alkaline geochemical signature (Pinto-Linares et al., 2008; Mascañano et al., 2013). Early mineralization stages are related to the skarn evolution, resulting in Cu-Au-Fe disseminated ore deposits (Gunnesch et al., 1994). This stage is characterized by pyrite, arsenopyrite, chalcopyrite, native bismuth and pyrrhotite as main ore minerals, and was succeeded by polymetallic Ag-Pb-Zn vein deposits (Gunnesch et al., 1994). The entire area is cross-cut by N-S extensional normal faults of the Taxco-San Miguel de Allende fault system, which controlled the emplacement of the La Paz Dyke System and associated hydrothermal Ag-Pb-Zn deposits (Castro-Larragoitia, 1990).

3. Methodology

3.1. Petrography and whole-rock geochemistry

Petrographic and whole-rock geochemical analysis were carried out in 27 samples of intrusive and skarn rocks, mostly obtained from underground drilling cores. Fifteen intrusive samples were collected, whereas twelve samples were obtained from the skarn. Major elements were measured with a PANalytical Axios Advanced wavelength dispersive XRF spectroscope at the GeoForschungsZentrum Potsdam (GFZ). Crushed and dried samples were melted down to tablets with lithium tetraborate metaborate (Fluxana FX-X65), with a sample to flux ratio of 1:6. The H₂O and CO₂ contents were determined with a Vario EL III (Elementar Analysensysteme GmbH, Hanau). The determination of the sulfur content was carried out by an ELTRA CS 200 (ELTRA GmbH, Neuss). Trace element analyses were performed at the Geoscience Center of the Georg-August-Universität Göttingen with a Perkin Elmer DRC II Inductively Coupled Mass Spectrometer (ICP-MS). Analyses were validated by repeated independent sample preparation, blanks and analyses of two different international reference standards. Results were analysed using the GCDkit 4.1 software (Janoušek et al., 2006, 2016).

3.2. Mineral chemistry

Thin sections were prepared and analyzed in the microprobe laboratory of the Geoscience Center of the Georg-August-Universität Göttingen. Thin sections were polished in two steps (3 und 1 μm) and vaporized with carbon. Measurements were carried out with a JEOL JXA 8900 RL wavelength dispersive electron microprobe in the microprobe laboratory at the GZG. Measurements allow a spot resolution of 1-2 μm and a detection limit of < 30 ppm. All elements with an atomic number $Z \geq 5$ can be measured.

3.3. Geochronology

3.3.1. U-Pb LA-ICP MS

U-Pb zircons ages were obtained for four intrusive rocks and two endoskarn samples at Stellenbosch University in South Africa. Samples were crushed and sieved and, afterwards, the mineral fractions were separated using conventional heavy liquid and isodynamic techniques. Zircon U-Pb dating was done with a Single Collector–Magnetic Sectorfield–Inductively Coupled Plasma–Mass Spectrometer (LA-SF-ICP-MS). A Resonetics Resolution S155 Excimer Laser in combination with a Finnigan Element 2 Mass Spectrometer was used. Detailed description of the methods for analysis and evaluation of the measurements can be found in Gerdes and Zeh (2006) and Frei and Gerdes (2009). Measurements were verified by using Plešovice (Sláma et al., 2008) and M127 (Nasdala et al., 2008; Mattinson, 2010) as standard zircon reference material. The calculation of concordia ages and concordia plots were carried out with the programme Isoplot 3.0 (Ludwig, 2003).

3.3.2. K-Ar

K-Ar biotite ages were determined in eight samples of intrusive rocks at the Geoscience Center of the Georg-August-Universität Göttingen. Samples were crushed and sieved in different grain size fractions depending on the size of the biotites. The biotite minerals were separated by standard techniques like magnetic separation and hand picking. The purity of the biotite separates was >99%. Purified biotites were ground in pure alcohol to remove altered rims that might have suffered a loss of Ar or K.

The argon isotopic composition was measured in a pyrex glass extraction and purification line coupled to a Thermo Scientific ARGUS VI noble gas mass spectrometer operating in static mode at the Geoscience Centre of the Georg-August-Universität Göttingen. The amount of radiogenic ^{40}Ar was determined by isotope dilution method using a highly enriched ^{38}Ar spike from Schumacher (1975). The spike is calibrated against the biotite standard HD-B1 (Fuhrmann et al., 1987). The age calculations are based on the constants recommended by the IUGS quoted in Steiger and Jäger (1977).

Potassium was determined in duplicate by flame photometry using a BWB-XP flame photometer. The samples were dissolved in a mixture of HF and HNO_3 according to the technique of Heinrichs and Herrmann (1990). The analytical error for the K/Ar age calculations is given on a 95% confidence level (2σ). Details of argon and potassium analyses for the laboratory in Göttingen are given in Wemmer (1991).

3.3.3. Re-Os

The Re-Os age was obtained in one molybdenite sample from the exoskarn of the Cobriza intrusion. For the Re measurement, the sample was cleaned chromatographically with TEVA Harz (Fa. Triskem) and measured with LA-ICP-MS, in alternation with the standard ARM 2007 (Markey et al., 2007). On the other hand, determination of ^{187}Os was performed with a Finnigan MAT 261 NTI-MS (Negative Thermal Ionization Mass Spectrometer), alternating sample and standard. The Re-Os age was calculated considering a ^{187}Re decay constant of $1.666 \times 10^{-11} \text{ a}^{-1}$ (Smoliar et al., 1996). For further details of sample preparation and analytical procedures, see Völkening et al. (1991), Walczyk et al. (1991) and Brauns (2001).

4. Results

4.1. Field observations and petrography

4.1.1. Intrusive rocks

All four intrusions of the Sierra del Fraile are porphyritic leucocratic igneous bodies that show holocrystalline, heterogranular textures. The groundmass consists of quartz and K-feldspar, whereas phenocrysts are hypidiomorphic to idiomorphic plagioclase (35-40%), xenomorphic quartz (20-25%), hypidiomorphic to xenomorphic K-feldspar (25-30%) and mafic minerals (biotite and hornblende, 10-15%). Plagioclase

phenocrysts show zoning and typical polysynthetic twins. Accessories are zircon, apatite and titanite/sphene.

The composition of the Membrillo, Santa Teresa and Dolores stocks is monzogranitic. In the Membrillo intrusion, plagioclase and biotite show alteration to sericite and chlorite, respectively. The Santa Teresa intrusion is cross-cut by a variety of mineralized veins, mostly filled with calcite, pyrite and chalcopyrite. Biotite shows slightly chloritisation. In the case of the Dolores intrusion, alteration of plagioclase, biotite and hornblende crystals increase from the centre to the rim of the pluton. At the rim of this igneous body, fractures mineralized with calcite and secondary formed pyrite can be observed. On the other hand, the Cobriza intrusion shows a monzogranitic to granodioritic composition. Like the samples from the Dolores intrusion, the alteration of the minerals increases from the centre to the rim of the intrusion. Calcite-mineralized fractures at the rim of the intrusion and secondary pyrite can be also observed.

4.1.2. Endoskarn

Endoskarns were only formed at the rim of the Dolores and Cobriza intrusions, showing thicknesses of up to 5 and 10 m, respectively. Excepting for scarce relics, the primary magmatic texture is no longer observable. Both at macro- and microscopic scale, endoskarns are medium-grained and equigranular to heterogranular. The composition of the endoskarn is highly variable and changes with the distance to the intrusion, which can be macroscopically noticed by a color change. It ranges from red, where garnet is the main mineral, to greenish gray, where pyroxene is the main mineral (Fig. 2a, b). The pyroxene content increases with the increasing distance to the intrusion, while the garnet content decreases.

Garnet, pyroxene and sulfides are the main minerals of the endoskarns. In thin section, hypidiomorphic to xenomorphic garnets are slightly reddish and present an average grain size of 0.25 mm. Xenomorphic pyroxene crystals with an average grain size of 0.4 mm are typically observed between garnets. Main sulphides are pyrite and subordinated chalcopyrite, which are mostly idiomorphic. The grain size of sulphides vary from ca. 0.1 mm to 3 mm. Carbonates are observable as well, occurring preferentially in veinlets (Fig. 2b). Though scarce, relic plagioclase and quartz crystals of the intrusion are present as well. Plagioclase alteration increases towards the wall-rock,

being incipient at the intrusion-endoskarn contact and profuse at the endoskarn-exoskarn contact.

4.1.3. Exoskarn

Macroscopically, exoskarn rocks are massive and fine-grained. The composition varies with increasing distance to the pluton, showing a garnet content decrease and a pyroxene content increase. Further away from the intrusion, the pyroxene content decreases again and the wollastonite content rises. Hence, colors range from red, where garnet is the mainly occurring mineral (Fig. 2c), over green-gray, with predominantly pyroxene composition, to white up to gray, where wollastonite is the dominant mineral. The sedimentary lamination is mostly overprinted and only locally observed (Fig. 2d).

At the microscopic scale, xenomorphic garnets show a variable grain size that decreases with increasing distance to the intrusion, reaching a maximum average of 0.5 mm close to the contact. Pyroxenes have a xenomorphic shape and an average grain size of approximately 0.4 mm. Samples of the outermost edge of the exoskarns show a retrograde mineral association with actinolite-tremolite. Large accumulations of sulphide ores can be found in the exoskarns, including pyrite, bornite, chalcopyrite, molybdenite, sphalerite and subordinated arsenopyrite (Fig. 2e, f). Also, carbonates are relic or filling of cavities.

4.2. Mineral chemistry

4.2.1. Intrusive rocks

Plagioclase crystals show an average composition of andesine in the Dolores (anorthite (An) = 37.70%, albite (Ab) = 60.19%, and orthoclase (Or) = 2.11%) and Cobriza intrusions (An = 35.32%, Ab = 62.36%, and Or = 2.32%) (Fig. 3). In both cases, only few analysis show oligoclase or labradorite compositions. Significant changes in composition perpendicular to the zonation were not observed. On the other hand, analyses of plagioclases from the Cobriza endoskarn and a fine-grained enclave of the Cobriza stock show similar andesine compositions (Fig. 3).

4.2.2. Endoskarn

Microprobe analyses were performed to determine the end-member composition of plagioclase, garnet and pyroxenes. Only fresh plagioclases of the Cobriza endoskarn

were analyzed, showing an average andesine composition (An = 39.59%, Ab = 59.05%, and Or = 1.36%) similar to plagioclases in the Cobriza monzogranite (Fig. 3). For pyroxenes, an average hedenbergite composition was obtained for samples of the Dolores endoskarn and exoskarn, and the Cobriza endoskarn (Fig. 4). As the Zn content was not measured, the determination of the end-member petedunnite ($\text{CaZnSi}_2\text{O}_6$) could not be evaluated. Therefore, only a distinction of Ca pyroxene between hedenbergite, diopside and johannsenite was possible. Finally, garnets of the Dolores endoskarn exhibit an average composition of andradite = 90.86%, grossular = 7.94%, uvarovite = 0.07% and pyralspite group = 1.14% (Fig. 5).

4.2.3. Exoskarn

Garnet and pyroxene compositions were determined for samples of the Dolores and Cobriza exoskarns. In the Dolores exoskarn, pyroxenes show a hedenbergite composition, similarly to the respective endoskarn. Hedenbergites of exoskarn, however, have a slightly higher Fe content (Fig. 4). Garnets have an almost identical composition to the endoskarn (andradite = 90.43%, grossular = 8.43%, uvarovite = 0.09% and pyralspite group = 1.14%), with a predominantly andraditic composition (Fig. 5). On the other hand, garnets of the Cobriza exoskarn show an average composition of andradite = 76.1%, grossular = 22.5%, uvarovite = 0.1% and pyralspite = 0.8% (Fig. 5), being thus slightly more enriched in Al and more depleted in Fe than garnets of the Dolores exoskarn.

4.3. Whole-rock geochemistry

Analytical results are displayed in Appendix 1. Data processing and plots were carried out using GCDkit 4.1 (Janoušek et al., 2006, 2016), including results from intrusions reported by Pinto-Linares et al. (2008).

4.3.1. Intrusive rocks

Intrusions show a relatively narrow range of SiO_2 content, varying between ca. 63 and 68 wt. %, though three samples of the Dolores intrusion show slightly higher values of around 72 wt. % (Table 1; Pinto-Linares et al., 2008). All samples show compositions that vary between granitic to granodioritic (Fig. 6a; Cox et al., 1979) and dominantly metaluminous to slightly peraluminous (Fig. 6b; Shand, 1943). Based on criteria of Frost

et al. (2001), the Sierra del Fraile stocks show dominant magnesian (Fig. 6c) and calc-alkalic compositions (Fig. 6d). Likewise, they mostly correspond to the high-K calc-alkaline series, with a slight tendency towards the shoshonite series (Peccerillo and Taylor, 1976).

Trace element patterns display a general steep negative slope in the primitive mantle-normalized plot, with marked negative anomalies of Nb-(Ta), P and Ti and positive anomalies of U and Pb (Fig. 7a) and enrichment in LILE with respect to HFSE. On the other hand, chondrite-normalized REE patterns show an enrichment in LREE with respect to HREE (Fig. 7b). A slightly to well-developed negative Eu anomaly is present in all samples (Fig. 7b), with Eu_N/Eu_N^* between 0.36 and 0.84 (Table 1), suggesting plagioclase fractionation. Moderate REE fractionation patterns are evident for most samples (Fig. 7b, Table 1), being slightly higher for those of the Cobriza intrusion ($25.14 \leq La_N/Yb_N \leq 43.27$; Table 1).

4.3.2. Skarn

Trace elements of both endoskarn and exoskarn rocks show a general depletion of LILE (K, Rb, Ba, Sr) and slightly enrichment in HFSE in comparison with intrusive rocks (Table 1, 2; Fig. 8a). Chondrite-normalized REE patterns show a general depletion of REE in skarn samples (Fig. 8b), though REE fractionation is comparable in skarn and intrusive rocks ($2.25 \leq La_N/Yb_N \leq 43.36$; Table 2).

If compared, Cu concentration increases from intrusive to exoskarn rocks (Fig. 9). A similar pattern is observed for other metals such as Fe, Ni, Sn, Sb, Zn, W and Bi (Table 1, 2), indicating that ore mineralizations are clearly concentrated in skarn, particularly exoskarn rocks.

4.4. Geochronology

4.4.1. U-Pb LA-ICP-MS

In all samples, cathodoluminescence images show zircons that are dominantly prismatic and exhibit oscillatory zoning, pointing to a magmatic origin (Fig. 10). Cores showing oscillatory or sector zoning are locally observed as well.

Concordant crystallization ages within the range of ca. 37.6-35.0 Ma were obtained for all samples, which also present zircon xenocrysts yielding Tonian, Devonian-Carboniferous and Cretaceous ages (Fig. 11, Appendix 1). Ages of 37.3 ± 0.3

and 36.8 ± 0.3 Ma were calculated for samples MGA and DQ76GD of the Membrillo and Santa Teresa stocks (Fig. 11a, 11b), respectively. Both the western Dolores intrusion (sample DJ14GR-2) and associated endoskarn (sample DO48SR-2) present comparable ages of 36.3 ± 0.3 and 36.2 ± 0.3 Ma (Fig. 11c, 11d), respectively. Likewise, zircons of the northwestern Cobriza intrusion (sample CO23-30GC) yield an age of 35.7 ± 0.3 Ma (Fig. 11e), similarly to the Cobriza endoskarn age of 35.3 ± 0.3 Ma (CO7801-20ENS) (Fig. 11f).

4.4.2. K-Ar

Results of K-Ar biotite ages for samples of the Santa Teresa, Dolores, and Cobriza intrusions are shown in Table 3. Due to extreme alteration, reliable biotite K-Ar ages for the Membrillo intrusion were not obtained. For the Santa Teresa intrusion, an age of 35.05 ± 0.89 Ma was determined. Ages of 35.43 ± 0.45 and 30.92 ± 0.41 Ma were obtained for the eastern Dolores intrusion, whereas an age of 35.07 ± 0.55 Ma was calculated for a sample of the eastern part. In the northwestern Cobriza stock, biotites yield two comparable ages of 34.23 ± 0.60 and 34.06 ± 0.59 Ma. Similarly, ages of 33.80 ± 0.36 and 27.13 ± 0.41 Ma were determined for the southeastern Cobriza stock.

4.4.3. Re-Os

Analytical results of Re-Os dating in molybdenites of the Cobriza exoskarn are presented in Table 4. An average molybdenite Re-Os age of 38.07 ± 0.27 Ma was obtained, being thus comparable with U-Pb ages obtained for the intrusions (Fig. 11).

5. Discussion

5.1. Petrogenesis of the Santa María de la Paz district magmatism

Worldwide, most significant Cu skarns are associated with Cu mineralized porphyries (Meinert et al., 2005). In Mexico, economically important Cu porphyry deposits were emplaced between the Upper Cretaceous and the Eocene, being intimately related to the Laramide Orogeny (Barton et al., 1995; Valencia-Moreno et al., 2017; Centeno-García, 2017). Intrusions and associated skarn deposits in the Sierra del Fraile, however, are younger and were interpreted as the result of the post-orogenic Laramide phase (Pinto-Linares et al., 2008; Mascuñano et al., 2013). Additionally, Pinto-Linares et al. (2008) indicated a transitional adakite-like to calc-alkaline geochemical signature for

the Sierra del Fraile magmatism, whereas Mascuñano et al. (2013) interpreted an affinity with high Ba-Sr granitoids.

Petrographic and whole-rock geochemical data (Section 4.1.1, 4.3) indicate that stocks of the Sierra del Fraile comprise granites and granodiorites with dominant metaluminous to slightly peraluminous, magnesian and calc-alkalic compositions, typical of Cordilleran granites (Frost et al., 2001). High-K calc-alkaline compositions (Peccerillo and Taylor, 1976) and negative Nb-(Ta), P and Ti anomalies further support a continental arc affinity.

Key features of both adakite and high Ba-Sr magmatism are the lack of Eu anomaly, high Sr/Y and La_N/Yb_N , and very low Y and Yb contents (Drummond and Defant, 1990; Martin, 1999; Fowler et al., 2001; Richards and Kerrich, 2007; Gómez et al., 2015; Lara et al., 2017). In contrast, most samples of the Sierra del Fraile intrusions show a negative Eu anomaly, whereas Sr/Y and La_N/Yb_N ratios, and Y and Yb contents are more similar to those recorded by normal arc rocks (Table 1, Fig. 12). Additionally, comparison with experimental data of Patiño Douce (1999) suggests an origin related to partial melting of mafic rocks and subordinated immature sediments (Fig. 13). The latter might account for zircon xenocrysts yielding variable Tonian to Cretaceous ages (Appendix 1).

Structural and geochronological data constrain the timing of the Laramide Orogeny at ca. 60 Ma for the study area (Tristán-González et al., 2009; Cuéllar-Cárdenas et al., 2012), thus supporting a post-Laramide setting for the Santa María de la Paz district magmatism, as previously indicated (Pinto-Linares et al., 2008; Mascuñano et al., 2013). Further Paleogene post-Laramide mineralizations are recorded in the region, constituting essentially skarn and epithermal deposits. Ag-Pb-Zn-Au veins in the Sierra de Catorce, immediately west of the Sierra del Fraile, are associated with granitoids yielding U-Pb zircon ages of ca. 45-40 Ma (Mascuñano et al., 2013). Contemporaneous magmatism and related Zn-Cu skarn mineralizations yielding a K-Ar orthoclase age of 43 ± 3 Ma were reported in the Charcas district (Mujica-Mondragón and Jacobo-Albarrán, 1983). Further west, Re-Os molybdenite ages of ca. 44-43 Ma constrain the timing of Zn-Pb-Cu-(Ag)±(Au) skarn and epithermal deposits of the San Martín district in the central Sierra Madre Occidental (Camprubí et al., 2015). In the Taxco district of the Sierra Madre del Sur, maximum U-Pb zircon and $^{40}\text{Ar}/^{39}\text{Ar}$ K-feldspar ages of ca. 35 Ma were obtained for Ag-Zn-Pb intermediate sulfidation epithermal deposits (Farfán-Panamá et al., 2015), thus being probably contemporaneous with the La Azul fluorite deposit, which presents

(U-Th)/He fluorite ages of ca. 33-30 Ma (Pi et al., 2005). Oligocene K-Ar whole-rock ages of ca. 31-29 Ma were also reported for intrusion-related mineralizations of the Fresnillo silver district in Zacatecas, southwest of San Luis Potosí (Lang et al., 1988).

Tectonic discrimination diagrams based on geochemical data are not conclusive, despite suggesting a possible continental arc setting (Fig. 14). It is thus argued that post-Laramide intrusions did not result from processes linked to the genesis of adakitic magmas or high Ba-Sr granitoids but, instead, from partial melting of mafic and subordinated Al-poor sediments that led to high-K calc-alkaline magmatism, typical of Cordilleran magmatism related to convergent settings (Patiño Douce, 1999; Frost et al., 2001). Though unclear, a possible mechanism for the genesis of the Santa María de la Paz district magmatism might imply post-Laramide slab removal of the Farallon slab that led to low-volume partial melting of a hydrated and fertile lithospheric mantle, which resulted from metasomatism during Laramide flat-slab subduction (Fig. 15; Humphreys, 1995, 2009; Ferrari et al., 1999, 2017). During ascent, magmas might also incorporate crustal rocks, as evidenced by zircon inheritance. Ferrari et al. (2017) indicated this mechanism as the most likely explanation for the middle to late Eocene magmatism of northeastern Mexico, thus accounting for the ca. 45-35 Ma post-Laramide magmatism and associated mineralizations of the region.

5.2. Skarn evolution and ore-forming processes

5.2.1. Temporal constraints

One of the most critical points to understand the genesis of ore deposits, particularly those related to skarns, is to provide robust temporal constraints, which essentially means to assess the timing and duration of ore-forming processes (e.g., Meinert et al., 2005; Chelle-Michou et al., 2015). Therefore, geochronological constraints on both skarn and intrusive rocks are required (Porter and Selby, 2010; Li et al., 2014; Chelle-Michou et al., 2015; Deng et al., 2015).

U-Pb LA-ICP-MS zircons ages obtained in stocks of the Sierra del Fraile are within the range of ca. 37.6-35.0 Ma (Section 4.1.1), being thus equivalent to previous geochronological constraints on these intrusions (Pinto-Linares et al., 2008; Mascuñano et al., 2013). Though slightly older, the Re-Os molybdenite age of 38.07 ± 0.27 Ma obtained for the Cobriza exoskarn is comparable to crystallization ages of the plutons, indicating the magma emplacement, skarn metasomatism and ore mineralization were

simultaneous (Zharikov, 1970), as recorded in other skarn deposits (Li et al., 2014; Chelle-Michou et al., 2015; Deng et al., 2015). During magma emplacement, skarn metasomatism triggered by fluid circulation might be slightly older than magma crystallization, thus accounting for the slightly differences between Re-Os molybdenite and U-Pb zircon ages.

On the other hand, closure temperatures for Re-Os in molybdenite and K-Ar in biotite were estimated at ca. 500°C and 350-300°C, respectively (Harrison et al., 1985; Grove and Harrison, 1996; Suzuki, 1996). The Re-Os age of the Cobriza exoskarn is more or less equivalent to zircon ages obtained in the Cobriza stock, whereas K-Ar biotite ages are slightly younger than their respective U-Pb zircon ages, showing differences of less than ca. 2 m.y. in most cases (Section 4.4). Only one K-Ar age of 27.13 ± 0.41 Ma is considerably younger and might result from partial Ar loss, as a second age of 33.80 ± 0.36 Ma was obtained for the same part of the pluton. Assuming a crystallization temperature of ca. 750-700°C for the intrusions and a closure temperature of ca. 360-380°C for Ar diffusion in biotites with an effective diffusive radius of 500 μm (Harrison et al., 1985; Grove and Harrison, 1996), cooling rates of ca. 0.2-0.3°C/k.y. can be estimated. Results thus point to a very fast cooling of intrusions, indicating shallow emplacement conditions.

5.2.2. Skarn characterization and ore deposition

Skarn-related magmatic rocks provide not only information to classify skarn deposits but also to characterize their genetic conditions (Meinert, 1992; Meinert et al., 2005). Geochronological data of the Santa María de la Paz district point to a shallow setting (Section 5.2.1), further supported by fluid inclusion data (Gunnesch et al., 1994), which is typical of Cu skarn deposits (Meinert, 1992; Meinert et al., 2005). On the other hand, geochemical data of stocks point to crustal high-K calc-alkaline magmas as the main source of mineralizations. The crustal fingerprint of magmas is also indicated by zircon inheritance (Appendix 1) and low Re contents in molybdenite (Table 4; Mao et al., 1999).

Skarn rocks of the Sierra del Fraile are quite different in their mineral composition (Section 4.1), showing a general zonation of five different mineral aggregate zones moving from the intrusion to the carbonate rocks:

1. Plagioclase- and quartz-rich zone with increasing alteration. Increasing amount of garnets and subordinated pyroxenes (endoskarn).
2. Garnet zone with continuous increasing amount of garnet (first exoskarn area).
3. Pyroxene zone with increasing amount of wollastonite and minor amount of garnets.
4. Wollastonite zone next to the carbonates with minor amount of garnet and pyroxene.
5. Marble or hornfels zone, depending on the wall-rock (limestone and shale, respectively).

Though pyroxene and garnet show significant variations in their relative abundances and grain size (Section 4.1), no significant changes are observed in their compositions (Fig. 3, 4). Hedenbergite and andradite compositions are dominant, as previously indicated for the Dolores skarn (Gunnesch et al., 1994), showing a slightly increase of Mg/Fe and Al/Fe, respectively, from the endoskarn to the exoskarn (Fig. 3, 4). The association of hedenbergite + pyrite together with the presence of pyrrhotite and the lack of magnetite-hematite (Gunnesch et al., 1994) suggest reducing and variable sulfidizing conditions, based on comparison with experimental data at 2 kbar and 300-600°C for the Ca-Si-Fe-O-S system (Burton et al., 1982; Gamble, 1982). Further evidence of low fO_2 is provided by the presence of sulfide-rich mineralizations with pyrite + chalcopyrite + native bismuth + pyrrhotite, resembling characteristics of reduced Au-Cu-Bi iron oxide deposits of the Tennant Creek Inlier, Australia (Skirrow and Walshe, 2002).

If compared with other Cu-Au skarns, skarns of the Sierra del Fraile show some singularities. Inferred reducing conditions are expected for gold but not for copper skarns, as the latter are typically more oxidized (Meinert et al., 2005). Pyroxene compositions are comparable to those of Au, Fe and W skarns, whereas garnets show compositions compatible with most skarn types (Einaudi and Burt, 1982; Meinert, 1992). Concerning Cu skarns, the main difference is the presence of hedenbergitic pyroxene, contrasting with typical diopside-dominated compositions (e.g.; Einaudi and Burt, 1982; Meinert, 1992). Andradite- and hedenbergite-dominated compositions were reported for the Changlongshan iron skarn of China (Xu and Lin, 2000) and tungsten skarn deposits of the Taebaeksan mineral district, South Korea (Park et al., 2017). On the other hand, Ni, V, Sc, Rb, Rb/Sr and Zr contents of the Sierra del Fraile intrusions

(Appendix 1) are similar to mean values of plutonic rocks associated with Cu skarns, though some parameters are also comparable to those of Zn, Au and Fe skarns (Meinert, 1995; Meinert et al., 2005).

Together with Cu and Au, for which the Sierra del Fraile skarns are exploited, high contents of other metals such as Fe, Ni, Sn, Sb, Zn, W and Bi are evident in skarn, particularly exoskarn rocks (Table 1, 2). Cu and Fe mineralizations are mainly related to pyrite, chalcopyrite and pyrrhotite, whereas Au is mainly contained in arsenopyrite and in minor amounts of Au tellurides (krennerite) (Gunnesch et al., 1994). However, Au is also associated with native bismuth (Gunnesch et al., 1994), which can be explained based on the capacity of Bi-melts to scavenge Au (Tooth et al., 2008, 2011). High Sb contents were also reported for the Sierra de Catorce (Tuta et al., 1988) and, together with Ag-Pb-Zn mineralizations, are mainly related to late vein deposits (Gunnesch et al., 1994). The presence of sphalerite would account for the high Zn contents. Though W and Sn contents cannot be easily explained by data, Paleocene-Eocene tungsten and Oligocene tin deposits, respectively, are common in central Mexico (Mead et al., 1988; Tuta et al., 1988).

Skarn deposits of the Sierra del Fraile have been typically considered as Cu-(Au) skarns (Gunnesch et al., 1994; Pinto-Linares et al., 2008), though they show some singularities, in terms such as their significant content in several base metals. Likewise, pyroxene and garnet skarn compositions and whole-rock geochemical data of related intrusions show some similarities with other Cu skarn deposits (Einaudi and Burt, 1982; Meinert, 1992, 1995; Meinert et al., 2005), though compositions show also an affinity with Au, Fe and Zn skarn types.

6. Conclusions

U-Pb LA-ICP-MS zircon data indicate crystallization ages of ca. 37.6-35.0 Ma for skarn-related stocks of the Sierra del Fraile. These granitic to granodioritic intrusions show dominant metaluminous to slightly peraluminous, high-K calc-alkaline compositions, resulting from magmas that were emplaced in a post-Laramide continental arc setting. Fast cooling rates of ca. 0.2-0.3°C/k.y. are estimated based on K-Ar biotite ages of ca. 35-33 Ma, which might indicate shallow emplacement conditions.

Skarn deposits were contemporaneous with emplacement and crystallization of stocks, as revealed by Re-Os molybdenite geochronological data of exoskarn rocks. Skarn rocks show a general depletion of LILE and REE and a slightly enrichment in HFSE in comparison with intrusive rocks. Pyroxene and garnet show dominant hedenbergite and andradite compositions, respectively. The association of hedenbergite, pyrite, chalcopyrite, native bismuth and pyrrhotite during skarn mineralization suggest reducing conditions, which are expected for Au but not for Cu skarns. Highest metal contents are restricted to skarn, particularly exoskarn rocks, including anomalies of Cu, Fe, Ni, Sn, Sb, Zn, W and Bi.

Comparison with other skarn deposits reveal some singularities for skarns of the Sierra del Fraile. Metal contents, ore minerals and environmental conditions, together with whole-rock geochemical data of stocks and pyroxene-garnet compositions, show similarities with both Cu and Au skarn deposits, despite of being also compatible with Fe, W, and Zn skarns. Hence, skarn and associated vein deposits of the Sierra del Fraile might have a high potential not only for Cu-(Au) but also for several base metals, as reported for comparable post-Laramide skarn and hydrothermal deposits of central and northern Mexico.

Acknowledgements

Observations of two anonymous reviewers as well as the editorial work of F. Pirajno and J. González-Jiménez are greatly acknowledged. The authors wish to thank A. Kronz for supervising microprobe analysis, K. Simon for ICP-MS geochemical data and M. Brauns for Re-Os molybdenite geochronological data. The authors are also grateful to the MSc Manuel González Ochoa and Negociación Minera de Santa Maria La Paz y Anexas for the logistical support and the facilities granted to work and take samples at the mine, and to the CONACyT (Project CB 130282) for the financial support. N. Rubinstein, A. Gómez and M. N. Maffini are acknowledged for fructiferous comments.

References

Albinson, T., Nelson, C.E., 2001. New mines and discoveries in Mexico and Central America. Special Publications of the Society of Economic Geologists, 8.

- Amato, J.M., Mack, G.H., Jonell, T.N., Seager, W.R., Upchurch, G.R., 2017. Onset of the Laramide orogeny and associated magmatism in southern New Mexico based on U-Pb geochronology. *Geol. Soc. Am. Bull.* doi: 10.1130/B31629.1
- Aranda-Gómez, J.J., McDowell, F.W., 1998. Paleogene extension in the southern Basin and Range Province of Mexico: Syn-depositional tilting of Eocene red beds and Oligocene volcanic rocks in the Guanajuato mining district. *Int. Geol. Rev.* 40, 116-134.
- Barboza-Gudiño, J.R., Torres-Hernández, J.R., Tristán-González, M., 1998. The Late Triassic – Early Jurassic active continental margin of western North America in northeastern Mexico. *Geofís. Int.* 37, 283–292.
- Barboza-Gudiño, J.R., Torres-Hernández, J.R., Tristán-González, M., 1999. Tectonic setting of pre-Oxfordian units from central and north-eastern Mexico. *Geol. Soc. Am. S.* 340, 197-210.
- Barboza-Gudiño, J.R., Hoppe, M., Gómez-Anguiano, M., Martínez-Marcás, P.R., 2004. Aportaciones para la interpretación estratigráfica y estructural de la porción noroccidental de la Sierra de Catorce, San Luis Potosí, México. *Rev. Mex. Cienc. Geol.* 21, 299-319.
- Barboza-Gudiño, J.R., Orozco-Esquivel, M.T., Gómez-Anguiano, M., Zavala-Monsiváis, A., 2008. The early Mesozoic volcanic arc of western North America in northeastern Mexico. *J. S. Am. Earth Sci.* 25, 49-63.
- Barboza-Gudiño, Zavala-Monsiváis, A., Venegas-Rodríguez, G., Barajas-Nigoche, L.D., 2010. Late Triassic stratigraphy and facies from northeastern Mexico: Tectonic setting and provenance. *Geosphere* 6, 621-640.
- Bartolini, C., Lang, H., Spell, T., 2003. Geochronology, geochemistry, and tectonic setting of the Mesozoic Nazas Arc in north-central Mexico, and its continuation to north South America. *AAPG Memoir* 79, 427-461.
- Barton, M.D., Staude, J.M.G., Zürcher, L., Megaw, P.K.M., 1995. Porphyry copper and other intrusion-related mineralization in Mexico, in: Peirce, F.W., Bolm, J.G. (Eds.), *Porphyry Copper Deposits from Alaska to Chile*. Arizona Geological Society Digest 20, pp. 487-524.
- Batchelor, R.A., Bowden, P., 1985. Petrogenetic interpretation of granitoid rock series using multicationic parameters. *Chem. Geol.* 48, 43-55.
- Blickwede, J.F., 1981. Stratigraphy and petrology of Triassic (?) “Nazas Formation”, Sierra de San Julian, Zacatecas, Mexico. M.Sc. Thesis, University of New Orleans.

- Boynton, W.V., 1984. Cosmochemistry of the rare earth elements: meteorite studies, in: Henderson, P. (Ed.), *Rare Earth Element Geochemistry*. Elsevier, Amsterdam, pp. 63-114.
- Brauns, C.M., 2001. A rapid, low-blank technique for the extraction of osmium from geological samples. *Chem. Geol.* 176, 379-384.
- Bunge, H.P., Grand, S.P., 2000. Mesozoic plate-motion history below the northeast Pacific Ocean from seismic images of the subducted Farallon slab. *Nature* 405, 337-340.
- Burton, J.C., Taylor, L.A., and Chou, I.-M., 1982. Determination of the fO_2 -T stability relations of hedenbergite and hedenbergite-johannsenite solid solutions by the hydrogen fugacity sensor technique. *Econ. Geol.* 77, 764-783.
- Camprubí, A., González-Partida, E., Valencia, V.A., Barra, F., 2015. Geochronology of Mexican mineral deposits. I: the San Martín polymetallic skarn, Zacatecas. *B. Soc. Geol. Mex.* 67, 119-122.
- Carrillo-Bravo, J., 1982. Exploración petrolera de la cuenca mesozoica del centro de México. *Bol. Asoc. Mex. Geol. Petrol.* 34, 21-46.
- Castro-Larragoitia, G.J., 1990. Investigaciones petrográficas y geoquímicas en el yacimiento de Ag-Pb-Zn-Cu de Santa María de la Paz, Matehuala, México. Diplomarbeit, Universität Karlsruhe.
- Centeno-García, E., 2017. Mesozoic tectono-magmatic evolution of Mexico: An overview. *Ore Geol. Rev.* 81, 1035-1052.
- Chelle-Michou, C., Chiaradia, M., Selby, D., Ovtcharova, M., Spikings, R.A., 2015. High-resolution geochronology of the Corocohuayco porphyry-skarn deposit, Peru: A rapid product of the Incaic Orogeny. *Econ. Geol.* 11, 423-443.
- Clark, K.F., Foster, C.T., Damon, P.E., 1982. Cenozoic mineral deposits and subduction-related magmatic arcs in Mexico. *Geol. Soc. Am. Bull.* 93, 533-544.
- Cox, K.G., Bell, J.D., Pankhurst, R.J., 1979. *The interpretation of igneous rocks*. Allen & Unwin, London.
- Cuéllar-Cárdenas M.A., Nieto-Samaniego, A.F., Levresse, G., Alaniz-Álvarez, S.A., Solari, L., Ortega-Obregón, C., López-Martínez, M., 2012. Límites temporales de la deformación por acortamiento Laramide en el centro de México. *Rev. Mex. Cienc. Geol.* 29, 179-203.
- Deng, X.-D., Li, J.-W., Wen, G., 2015. U-Pb geochronology of hydrothermal zircons from the Early Cretaceous iron skarn deposits in the Handan-Xingtai district, North China Craton. *Econ. Geol.* 110, 2159-2180.

- Dickinson, W.R., Snyder, W.S., 1978. Plate tectonics of the Laramide Orogeny. *Geol. Soc. Am. Mem.* 151, 355-366.
- Drummond, M.S., Defant, M.J., 1990. A model for trondhjemite-tonalite-dacite genesis and crustal growth via slab melting: Archean to modern comparisons. *J. Geophys. Res.* 95, 21503-21521.
- Einaudi, M.T., 1981. Skarn deposits. *Econ. Geol.* 75, 317-391.
- Einaudi, M.T., Burt, D.M., 1982. Introduction - Terminology, classification, and composition of skarn deposits. *Econ. Geol.* 77, 745-754.
- Eguiluz-de Antuñano, S., Aaranda-García, M., Marrett, R., 2000. Tectónica de la Sierra Madre Oriental, México. *Bol. Soc. Geol. Mex.* 53, 1-26.
- Farfán-Panamá, J.L., Camprubí, A., González-Partida, E., Iriondo, A., González-Torres, E., 2015. Geochronology of Mexican mineral deposits. III: the Taxco epithermal deposits, Guerrero. *B. Soc. Geol. Mex.* 67, 357-366.
- Ferrari, L., López-Martínez, M., Aguirre-Díaz, G., Carrasco-Núñez, G., 1999. Space-time patterns of Cenozoic arc volcanism in central Mexico: From the Sierra Madre Occidental to the Mexican Volcanic Belt. *Geology* 27, 303-306.
- Ferrari, L., Orozco-Esquivel, T., Bryan, S.E., López-Martínez, M., Silva-Fragoso, A., 2017. Cenozoic magmatism and extension in western Mexico: Linking the Sierra Madre Occidental silicic large igneous province and the Comundú Group with the Gulf of California rift. *Earth-Sci. Rev.* <http://dx.doi.org/10.1016/j.earscirev.2017.04.006>
- Fowler, M.B., Henney, P.J., Darbyshire, D.P.F., Greenwood, P.B., 2001. Petrogenesis of high Ba-Sr granites: the Rogart pluton, Sutherland. *J. Geol. Soc. London* 158, 521-534.
- Frei, D., Gerdes, A., 2009. Precise and accurate in situ U-Pb dating of zircon with high sample throughput by automated LA-SF-ICPMS. *Chem. Geol.* 261, 261-270.
- Frost, B.R., Calving, G.B., Collins, W.J.R., Arculus, R.J., Ellis, D.J., Frost, C.D., 2001. A geochemical classification for granitic rocks. *J. Petrol.* 42, 2033-2048.
- Fuhrmann, U., Lippolt, H.J., Hess, J.C., 1987. Examination of some proposed K-Ar standards: $^{40}\text{Ar}/^{39}\text{Ar}$ analyses and conventional K-Ar-data. *Chem. Geol.* 66, 41-51.
- Gamble, R.P., 1982. An experimental study of sulfidation reactions involving andradite and hedenbergite. *Econ. Geol.* 77, 784-797.
- Gerdes, A., Zeh, A., 2006. Combined U-Pb and Hf isotope LA-(MC)-ICP-MS analyses of detrital zircons: Comparisons with SHRIMP and new constraints for the

- provenance and age of an Armorican metasediment in central Germany. *Earth Planet. Sci. Lett.* 249, 47-61.
- Gómez, A.L.R., Rubinstein, N.A., Valencia, V.A., 2015. Gondwanan magmatism with adakite-like signature linked to Cu (Mo)-porphyry deposits from the San Rafael Massif, Medoza Province, Argentina. *Chem. Erde – Geochem.* 75, 89-104.
- Grove, M., Harrison, T.M., 1996. $^{40}\text{Ar}^*$ diffusion in Fe-rich biotite. *Am. Mineral.* 81, 940-951.
- Guzmán, E.J., de Cserna, Z., 1963. Tectonic history of Mexico. *AAPG Memoir* 2, 113-129.
- Gunnesch, K.A., Torres del Ángel, C., Cuba Castro, C., Sáez, J., 1994. The Cu-(Au) skarn and Ag-Pb-Zn vein deposits of La Paz, northeastern Mexico: Mineralogic, paragenetic, and fluid inclusion characteristics. *Econ. Geol.* 89, 1640-1650.
- Harrison, T.M., Duncan, I., McDougall, I., 1985. Diffusion of ^{40}Ar in biotite: Temperature, pressure and compositional effects. *Geochim. Cosmochim. Acta* 49, 2461-2468.
- Heinrichs, H., Herrmann, A.G., 1990. *Praktikum der Analytischen Geochemie*. Springer, Berlin Heidelberg.
- Humphreys, E., 1995. Post-Laramide removal of the Farallon slab, western United States. *Geology* 23, 987-990.
- Humphreys, E., 2009. Relation of flat subduction to magmatism and deformation in the western United States. *Geol. Soc. Am. Mem.* 204, 85-98.
- Hoppe, M., Barboza-Gudiño, J.R., Schulz, H.M., 2002. Late Triassic submarine fan in northwestern San Luis Potosí, Mexico – Lithology, facies and diagenesis. *Neues Jahrb. Geol. P. M.* 12, 705-724.
- Izaguirre, A., Camprubí, A., Iriondo, A., 2017. Mesozoic orogenic gold deposits in Mexico. *Ore Geol. Rev.* 81, 1172-1183.
- Janoušek, V., Farrow, C.M., Erban, V., 2006. Interpretation of whole-rock geochemical data in igneous geochemistry: introducing Geochemical Data Toolkit (GCDkit). *J. Petrol.* 47, 1255-1259.
- Janoušek, V., Moyen, J.-F., Martin, H., Erban, V., Farrow, C., 2016. *Geochemical modelling of igneous processes – Principles and recipes in R language*. Springer, Berlin Heidelberg.
- Lang, B., Steinitz, G., Sawkins, F.J., Simmons, S.F., 1988. K-Ar age studies in the Fresnillo silver district, Zacatecas, Mexico. *Econ. Geol.* 83, 1642-1646.
- Lara, P., Oyhantçabal, P., Dadd, K., 2017. Post-collisional, Late Neoproterozoic, high-Ba-Sr granitic magmatism from the Dom Feliciano Belt and its cratonic foreland,

- Uruguay: Petrography, geochemistry, geochronology, and tectonic implications. *Lithos* 277, 178-198.
- Li, S., Yang, X., Huang, Y., Sun, W., 2014. Petrogenesis and mineralization of the Fenghuangshan skarn Cu-Au deposit, Tongling ore cluster field, Lower Yangtze metallogenic belt. *Ore Geol. Rev.* 58, 148-162.
- López-Doncel, R., 2003. La Formación Tamabra del Cretácico Medio en la porción central del margen occidental de la plataforma Valles - San Luis Potosí, centro-noreste de México. *Rev. Mex. Cienc. Geol.* 20, 1-19.
- López-Infanzón, M., 1986. Estudio petrogenético de las rocas ígneas en las formaciones Huizachal y Nazas. *Bol. Soc. Geol. Mex.* 47, 1-42.
- Ludwig, K.R. 2003. Isoplot 3.00, a geochronological toolkit for Microsoft Excel. Berkeley Geochronology Center, Berkeley.
- Mao, J., Zhang, Z., Zhang, Z., Du, A., 1999. Re-Os isotopic dating of molybdenites in the Xiaoliugou W (Mo) deposit in the northern Qilian mountains and its geological significance. *Geochim. Cosmochim. Acta* 63, 1815-1818.
- Markey, R., Stein, J., Hannah, J.L., Zimmerman, A., Selby, D., Creaser, R.A., 2007. Standardizing Re-Os geochronology: A new molybdenite Reference Material (Henderson, USA) and the stoichiometry of Os salts. *Chem. Geol.* 244, 74-87.
- Martin, H., 1999. Adakitic magmas: modern analogues of Archaean granitoids. *Lithos* 46, 411-429.
- Mascuñano, E., Levresse, G., Cardellach, E., Tritlla, J., Corona-Esquivel, R., Meyzen, C., 2013. Post-Laramide, Eocene magmatic activity in Sierra de Catorce, San Luis Potosí, México. *Rev. Mex. Cienc. Geol.* 30, 299-311.
- Mattinson, J.M., 2010. Analysis of the relative decay constants of ^{235}U and ^{238}U by multi-step CA-TIMS measurements of closed-system natural zircon samples. *Chem. Geol.* 275, 186-198.
- McDonough, W.F., Sun, S.-S., 1995. Composition of the Earth. *Chem. Geol.* 120, 223-253.
- Mead, R.D., Kesler, S.E., Foland, K.A., Jones, L.M., 1988. Relationship of Sonoran tungsten mineralization to the metallogenic evolution of Mexico. *Econ. Geol.* 83, 1943-1965.
- Meinert, L.D., 1992. Skarns and skarn deposits. *Geosci. Can.* 19, 145-162.
- Meinert, L.D., 1995. Compositional variation of igneous rocks associated with skarn deposits – Chemical evidence for a genetic connection between petrogenesis and

- mineralization. Mineralogical Association of Canada Short Course Series 23, 401-418.
- Meinert, L.D., Dipple, G.M., Nicolescu, S., 2005. World skarn deposits. *Econ. Geol.* 100, 299-336.
- Meschede, M., Frisch, W., Herrmann, U.R., Ratschbacher, L., 1997. Stress transmission across an active plate boundary: An example from southern Mexico. *Tectonophysics* 266, 81-100.
- Miyashiro, A., 1978. Nature of alkali volcanic rock series. *Contrib. Mineral. Petrol.* 66, 91-104.
- Morimoto, N., 1988. Nomenclature of pyroxenes. *Mineral. Petrol.* 39, 55-76.
- Mújica-Mondragón, R., Jacobo-Albarrán, J., 1983. Estudio petrogenético de las rocas ígneas y metamórficas del Altiplano Mexicano. Instituto Mexicano del Petróleo, Subdirección Técnica de Exploración, Proyecto C-1156, informe técnico (inédito).
- Nasdala, L., Hofmeister, W., Norberg, N., Mattinson, J.M., Corfu, F., Dörr, W., Kamo, S.L., Kennedy, A.K., Kronz, A., Reiners, P.W., Frei, D., Košler, J., Wan, Y., Götze, J., Häger, T., Kröner, A., Valley, J.W., 2008. Zircon M257–A homogeneous natural reference material for the ion microprobe U-PB analysis of zircon. *Geostand. Geoanal. Res.* 32, 247-265.
- Nieto-Samaniego, A.F., Alaniz-Álvarez, S.A., Camprubí, A., 2007. Mesa Central of Mexico: Stratigraphy, structure, and Cenozoic tectonic evolution. *Geol. Soc. Am. S.* 422, 41-70.
- Pantoja-Alor, J., 1972. La Formación Nazas del levantamiento de Villa Juárez, Estado de Durango. II Convención Nacional de la Sociedad Geológica Mexicana, Memorias, 25-31.
- Park, C., Choi, W., Kim, H., Park, M.-H., Kang, I.-M., Lee, H.-S., Song, Y., 2017. Oscillatory zoning in skarn garnet: Implications for tungsten ore exploration. *Ore Geol. Rev.* <https://doi.org/10.1016/j.oregeorev.2017.08.003>
- Patiño-Douce, A.E., 1999. What do experiments tell us about the relative contribution of crust and mantle to the origin of granitic magmas?, in: Castro, A., Fernández, C., Vigneresse, J.L. (Eds.), *Understanding granites: Integrating new and classical techniques*. Geological Society, London, Special Publications, 168, pp. 55-75.
- Pearce, J.A., Harris, N.W., Tindle, A.G., 1984. Trace element discrimination diagrams for the tectonic interpretation of granitic rocks. *J. Petrol.* 25, 956-983.

- Peccerillo, A., Taylor, S.R., 1976. Geochemistry of Eocene calc-alkaline volcanic rocks from the Kastamonu area, Northern Turkey. *Contrib. Mineral. Petrol.* 58, 63-81.
- Pi, T., Solé, J., Taran, Y., 2005. (U-Th)/He dating of fluorite: application to the La Azul fluorite deposit in the Taxco mining district, Mexico. *Miner. Deposita* 39, 976-982.
- Pinto-Linares, P.J., 2008. Geología y génesis de la mineralización económica en el distrito minero de La Paz, S.L.P., México. Ph.D. Thesis, Universidad Nacional Autónoma de México.
- Pinto-Linares, P.J., Levrresse, G., Tritlla, J., Valencia, V.A., Torres-Aguilera, J.M., González, M., Estrada, D., 2008. Transitional adakite-like to calc-alkaline magmas in a continental extensional setting at La Paz Au-Cu skarn deposits, Mesa Central, Mexico. *Rev. Mex. Cienc. Geol.* 25, 39-58.
- Porter, S.J., Selby, D., 2010. Rhenium-Osmium (Re-Os) molybdenite systematics and geochronology of the Cruachan Granite skarn mineralization, Etive Complex: implications for emplacement chronology. *Scot. J. Geol.* 46, 17-21.
- Richards, J.P., Kerrich, R., 2007. Adakite-like rocks: Their diverse origins and questionable role in metallogenesis. *Econ. Geol.* 102, 537-576.
- Schumacher, E., 1975. Herstellung von 99,9997% ^{38}Ar für die $^{40}\text{K}/^{40}\text{Ar}$ Geochronologie. *Geochron. Chimia* 24, 441-442.
- Shand, S.J., 1943. Eruptive rocks. Their genesis, composition, classification, and their relation to ore-deposits with a chapter on meteorite. John Wiley & Sons, New York.
- Skirrow, R.G., Walshe, J.L., 2002. Reduced and oxidized Au-Cu-Bi iron oxide deposits of the Tennant Creek Inlier, Australia: An integrated geologic and chemical model. *Econ. Geol.* 97, 1167-1202.
- Sláma, J., Košler, J., Condon, D.J., Crowley, J.L., Gerdes, A., Hanchar, J.M., Horstwood, M.S.A., Morris, G.A., Nasdala, L., Norberg, N., Schaltegger, U., Schoene, B., Tubrett, M.N., Whitehouse, M.J., 2008. Plešovice zircon – a new natural reference material for U-Pb and Hf isotopic microanalysis. *Chem. Geol.* 249, 1-35.
- Smoliar, M.I., Walker, R.J., Morgan, J.W., 1996. Re-Os isotope constraints on the age of Group IIA, IIIA, IVA, and IVB iron meteorites. *Science* 271, 1099-1102.
- Steiger, R.H., Jäger, E., 1977. Subcommittee on geochronology: convention on the use of decay constants in geo and cosmochronology. *Earth Planet. Sci. Lett.* 36, 359-362.

- Suzuki, K., Shimizu, H., Masuda, A., 1996. Re-Os dating of molybdenites from ore deposits in Japan: Implication for the closure temperature of the Re-Os system for molybdenite and the cooling history of molybdenum ore deposits. *Geochim. Cosmochim. Acta* 60, 3151-3159.
- Tooth, B., Brugger, J., Ciobanu, C., Liu, W., 2008. Modeling of gold scavenging by bismuth melts coexisting with hydrothermal fluids. *Geology* 36, 815-818.
- Tooth, B., Ciobanu, C., Green, L., O'Neill, B., Brugger, J., 2011. Bi-melt formation and gold scavenging from hydrothermal fluids: An experimental study. *Geochim. Cosmochim. Acta* 75, 5423-5443.
- Tristán-González, M., Aguirre-Díaz, G.J., Labarthe-Hernández, G., Torres-Hernández, J.R., Bellon, H., 2009. Post-Laramide and pre-Basin and Range deformation and implications for Paleogene (55–25 Ma) volcanism in central Mexico: A geological basis for a volcano-tectonic stress model. *Tectonophysics* 471, 136-152.
- Tuta, Z.H., Sutter, J.F., Kesler, S.E., Ruiz, J., 1988. Geochronology of mercury, tin and fluorine mineralization in northern Mexico. *Econ. Geol.* 83, 1931-1942.
- Valencia-Moreno, M., Ochoa-Landín, L., Noguez-Alcántara, B., Ruiz, J., Pérez-Segura, E., 2006. Características metalogenéticas de los depósitos de tipo pórfido cuprífero en México y su situación en el contexto mundial. *Bol. Soc. Geol. Mex.*, 1-26.
- Valencia-Moreno, M., Camprubí, A., Ochoa-Landín, L., Calmus, T., Mendivil-Quijada, H., 2017. Latest Cretaceous-early Paleogene “boom” of porphyry Cu mineralization associated with the Laramide magmatic arc of Mexico. *Ore Geol. Rev.* 81, 1113-1124.
- Völkening, J., Walczyk, T., Heumann, K.G., 1991. Osmium isotope ratio determinations by negative thermal ionization mass spectrometry. *Int. J. Mass Spectrom.* 105, 147-159.
- Walczyk, T., Hebeda, E.H., Heumann, K.G., 1991. Osmium isotope ratio measurements by negative thermal ionization mass spectrometry (NTI-MS). *Fresen. J. Anal. Chem.* 341, 537-541.
- Wemmer, K., 1991. K/Ar-Altersdatierungsmöglichkeiten für retrograde Deformationsprozesse im spröden und duktilen Bereich - Beispiele aus der KTB-Vorbohrung (Oberpfalz) und dem Bereich der Insubrischen Linie (N-Italien). *Göttinger Arbeiten zur Geologie und Paläontologie* 51, 1-61.
- Xu, G., Lin, X., 2000. Geology and geochemistry of the Changlongshan skarn iron deposit, Anhui Province, China. *Ore Geol. Rev.* 16, 91-106.

Zharikov, V.A., 1970. Skarns. *Int. Geol. Rev.* 12, 541-559.

Zharikov, V.A., Rusinov, V.L., Marakushev, A.A., Zaraisky, G.P., Omelianenko, B.I., Pertsev, N.N., Rass, I.T., Andreeva, O.V., Abramov, S.S., Podlessky, K.V., Shapovalov, Y.B., Seredkin, M.S., Golovina, V.A., 1998. *Metasomatism and metasomatic rocks*. Nauchnyi Mir, Moscow.

Fig. 1. Geological map of the Santa María de la Paz district in the Sierra de Fraile.

Fig. 2. Representative drill core (a-d), hand specimen (e) and thin section (f) samples of Sierra del Fraile skarn rocks. a) Dolores endoskarn, showing altered remnants of the intrusion (lower part), pyroxene and disseminated pyrite. b) Cobriza endoskarn, mostly dominated by pyroxene and late calcite veinlets. c). Dolores exoskarn, consisting mostly of garnet and subordinated pyroxene. d). Dolores exoskarn close to the wall rock, showing garnet replacement (upper part) and relics of the primary bedding in limestone (lower part). e). Ore-bearing Cobriza skarn made up of pyrite, bornite and subordinated arsenopyrite. f) Photomicrograph (reflected light) of ore minerals in the Dolores exoskarn. Py: pyrite, Px: pyroxene, Cal: calcite, Grt: garnet, Apy: arsenopyrite, Bn: bornite.

Fig. 3. Ternary classification of feldspars of intrusion (Dolores and Cobriza) and endoskarn samples (Cobriza).

Fig. 4. Classification of pyroxenes from different skarn samples in a) the quaternary Ca-Fe-Mg-system after Morimoto (1988) and b) ternary Ca-system.

Fig. 5. Classification of garnets from different skarn samples in the ternary Ca-garnet-pyralspite-system.

Fig. 6. Major element results for the Sierra del Fraile intrusive rocks of this study (circles) and Pinto-Linares et al. (2008) (triangles). Dolores intrusion: red, Cobriza intrusion: yellow, Membrillo intrusion: light blue, Santa Teresa intrusion: blue. a) TAS classification diagram after Cox et al. (1979). Alkaline and subalkaline/tholeiitic fields after Miyashiro (1978). The circles represent the data of this work and the squares of the previous work by Pinto-Linares et al. (2008). b) A/CNK vs A/NK plot after Shand (1943). c) SiO_2 vs Fe^* index = $\text{FeO}t/(\text{FeO}t + \text{MgO})$ after Frost et al. (2001). d) SiO_2 vs MALI index = $\text{Na}_2\text{O} + \text{K}_2\text{O} - \text{CaO}$ after Frost et al. (2001). e) K_2O vs. SiO_2 diagram after Peccerillo and Taylor (1976).

Fig. 7. Trace element results for the Sierra del Fraile intrusive rocks of this study (circles) and Pinto-Linares et al. (2008) (triangles). Dolores intrusion: red, Cobriza intrusion: yellow, Membrillo intrusion: light blue, Santa Teresa intrusion: blue. a) Primitive mantle-normalized multielement plot (primitive mantle composition after

McDonough and Sun, 1995). b) Chondrite-normalized REE plot (chondrite composition after Boynton, 1984).

Fig. 8. Trace element results for the Sierra del Fraile endoskarn (x) and exoskarn (+) rocks. Grey areas indicate composition of intrusive rocks of Fig. 6. Dolores intrusion: red, Cobriza intrusion: yellow, Santa Teresa intrusion: blue. a) Primitive mantle-normalized multielement plot (primitive mantle composition after McDonough and Sun, 1995). b) Chondrite-normalized REE plot (chondrite composition after Boynton, 1984).

Fig. 9. Boxplot of Cu contents (ppm) for intrusive, endoskarn and exoskarn rocks of the Sierra del Fraile. Note that $[Cu]_{intrusions} < [Cu]_{endoskarn} < [Cu]_{exoskarn}$.

Fig. 10. Cathodoluminescence images of representative zircons with individual $^{206}Pb/^{238}U$ ages and respective 2σ errors (sample CO23-30GC).

Fig. 11. U-Pb diagrams. Red and green ellipses indicate data used for age calculations and concordia age, respectively. Errors depicted at the 2σ level. Analytical data are presented in Appendix 1.

Fig. 12. Y vs Sr/Y diagram showing fields for arc calc-alkaline and adakite-like rocks after Drummond and Defant (1990). Circles: this study, triangles: Pinto-Linares et al. (2008). Dolores intrusion: red, Cobriza intrusion: yellow, Membrillo intrusion: light blue, Santa Teresa intrusion: blue.

Fig. 13. $Al_2O_3 + Fe_2O_3 + MgO + TiO_2$ vs $Al_2O_3 / (Fe_2O_3 + MgO + TiO_2)$ diagram showing compositions of intrusions of the Sierra del Fraile, including fields of melt compositions experimentally generated by melting of various lithologies after Patiño-Douce (1999). Circles: this study, triangles: Pinto-Linares et al. (2008). Dolores intrusion: red, Cobriza intrusion: yellow, Membrillo intrusion: light blue, Santa Teresa intrusion: blue.

Fig. 14. Tectonic discrimination diagrams based on geochemical data. Circles: this study, triangles: Pinto-Linares et al. (2008). Dolores intrusion: red, Cobriza intrusion: yellow, Membrillo intrusion: light blue, Santa Teresa intrusion: blue. a) Y + Nb vs Rb diagram after Pearce et al. (1984). b) R_1 vs R_2 diagram after Batchelor and Bowden (1985).

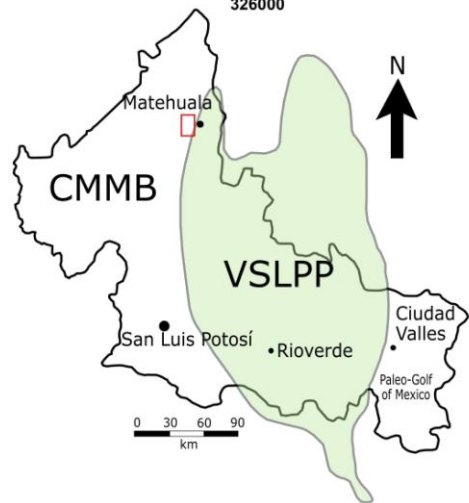
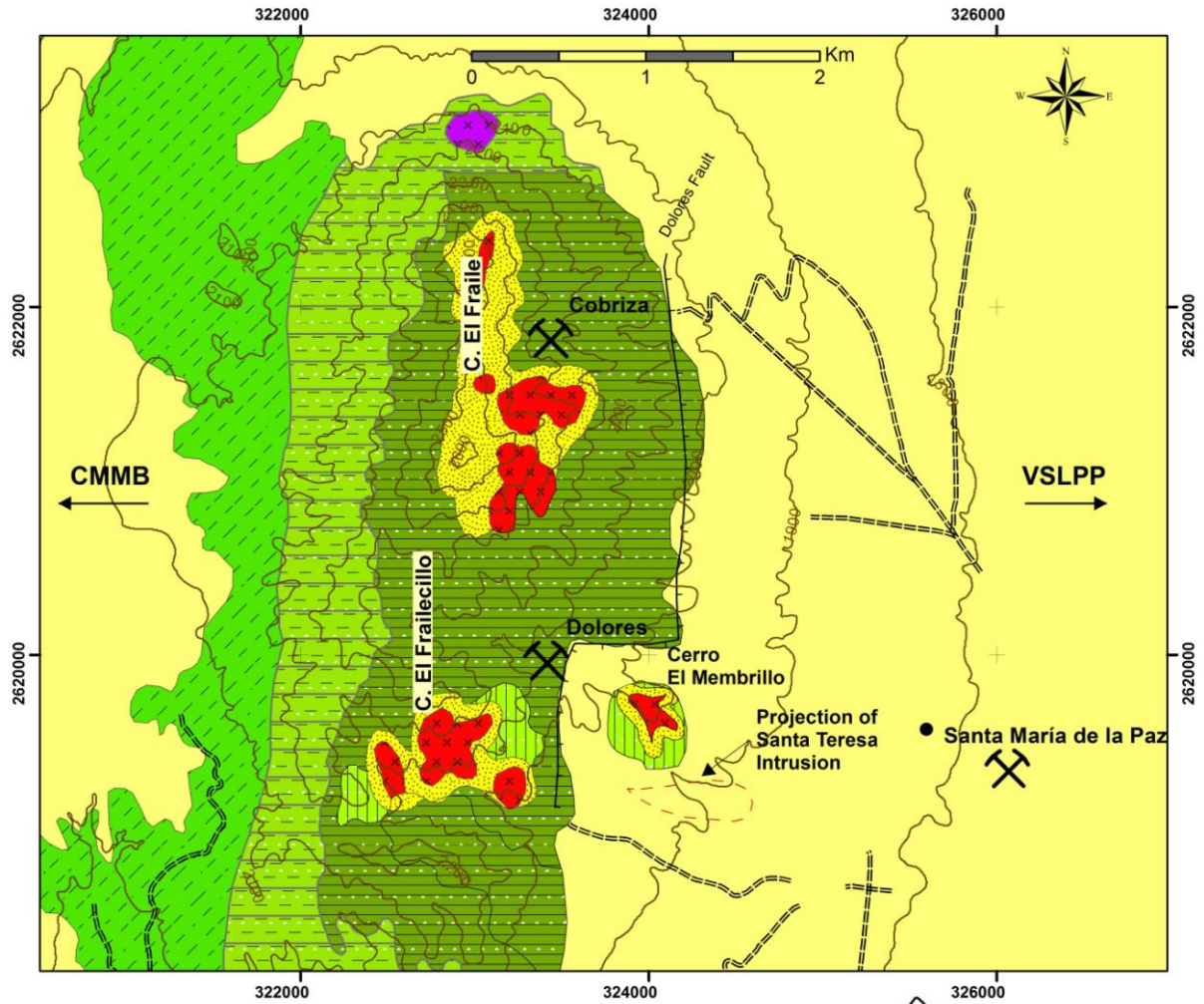
Fig. 15. Tectonic and geodynamic scenario for petrogenesis of the Sierra del Fraile magmatism (modified after Ferrari et al., 2017), showing schematically the most likely setting for the genesis of the Santa María de la Paz district magmatism. Post-Laramide slab removal of the Farallon slab led to low-volume partial melting of a hydrated and fertile lithospheric mantle, which resulted from previous metasomatism during Laramide flat-slab subduction (Humphreys, 1995, 2009; Ferrari et al., 1999, 2017). See Section 5.1 for further discussion.

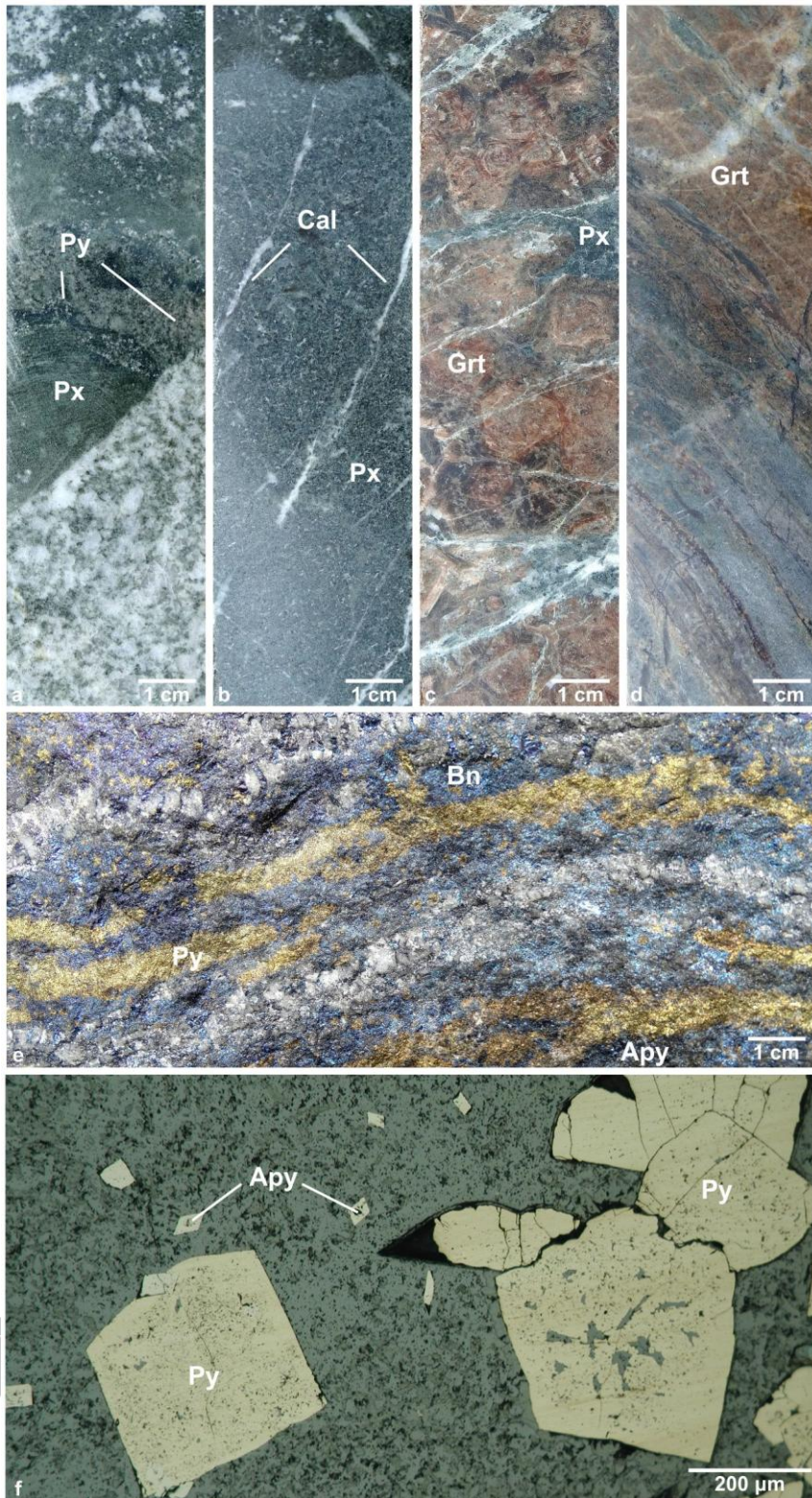
Table 1. Results of major and trace element analyses of intrusive rocks in the Sierra del Fraile. $Eu^* = \sqrt{Sm_N \times Gd_N}$. Chondrite-normalized values after Boynton (1984).

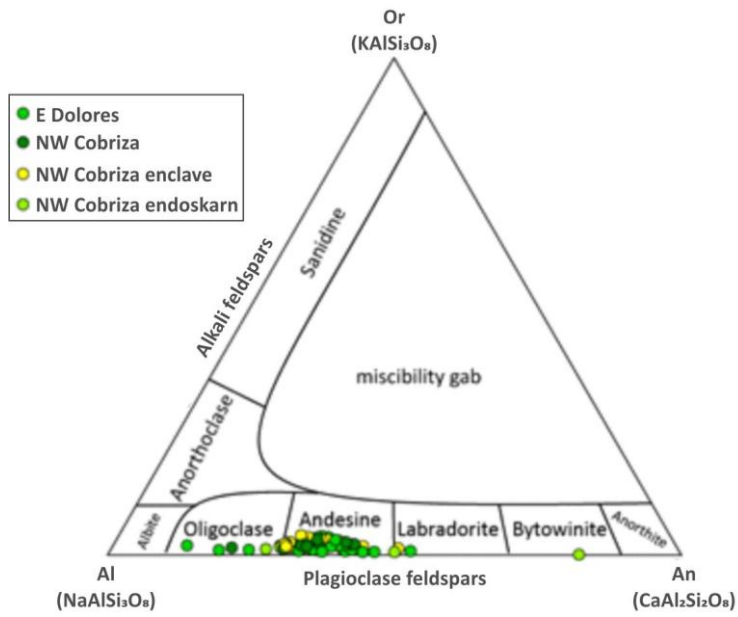
Table 2. Results of major and trace element analyses of skarn rocks in the Sierra del Fraile. $Eu^* = \sqrt{Sm_N \times Gd_N}$. Chondrite-normalized values after Boynton (1984).

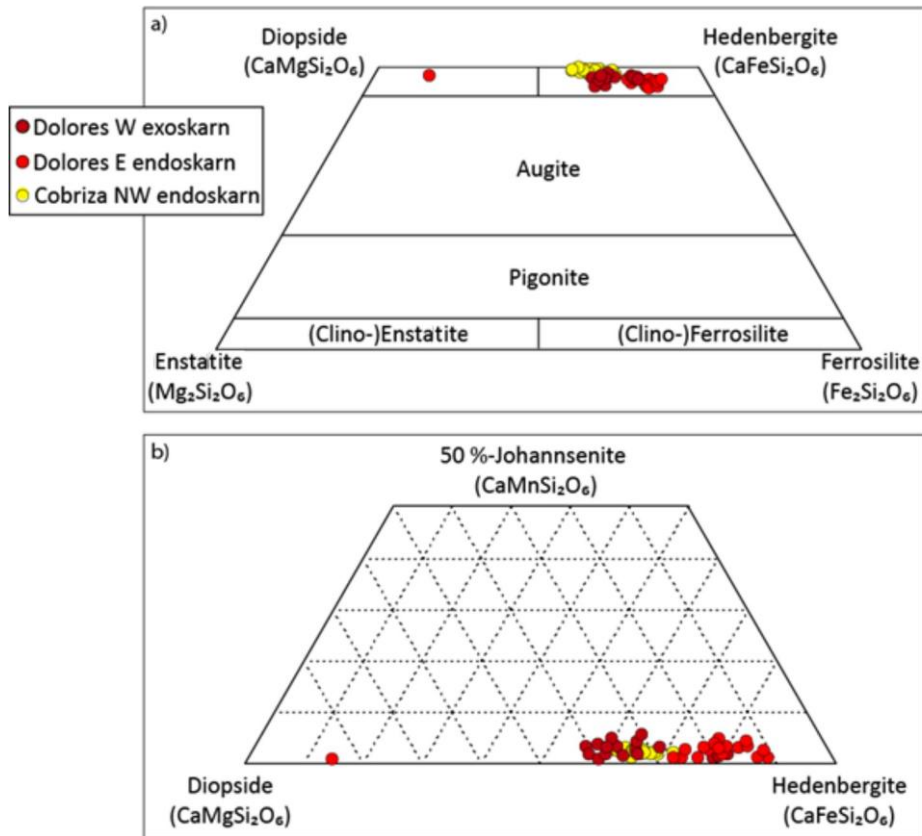
Table 3. Results of K-Ar age determinations in biotites of intrusive rocks.

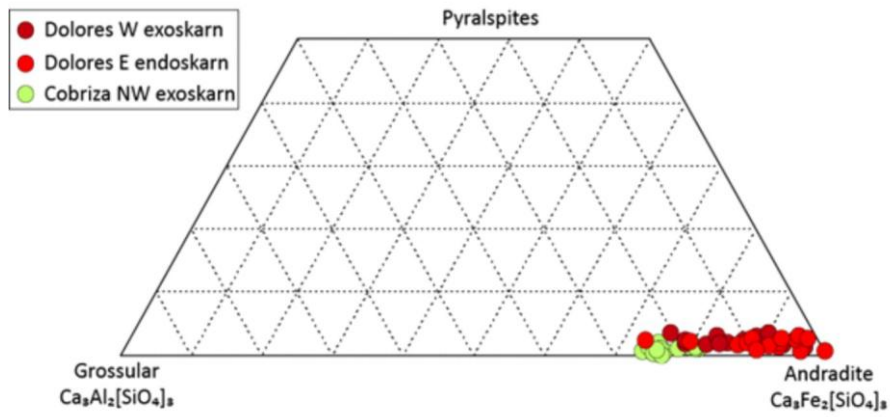
Table 4. Results of the Re-Os age determination ($\pm 2\sigma$) in molydonites of the Cobriza exoskarn. Age determinations of the ARM 2007 standard (Markey et al., 2007) are presented as well.

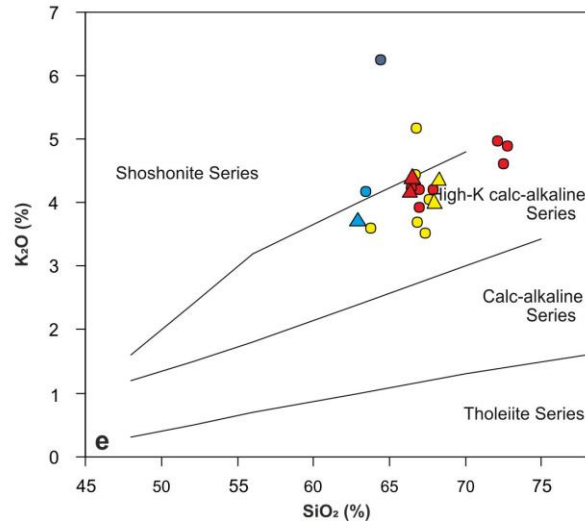
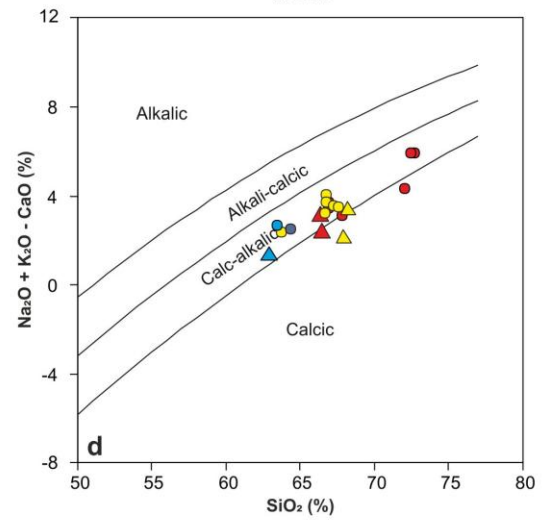
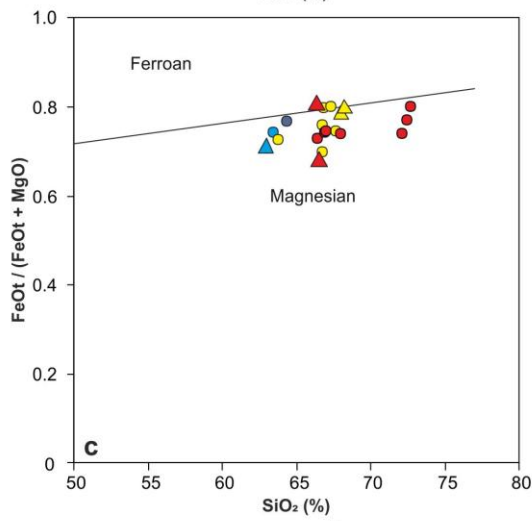
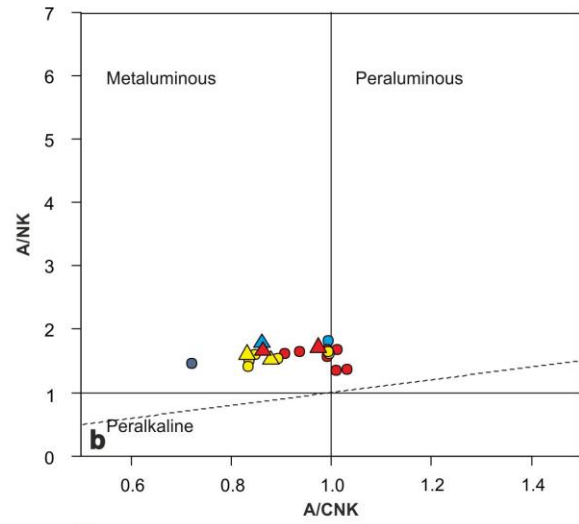
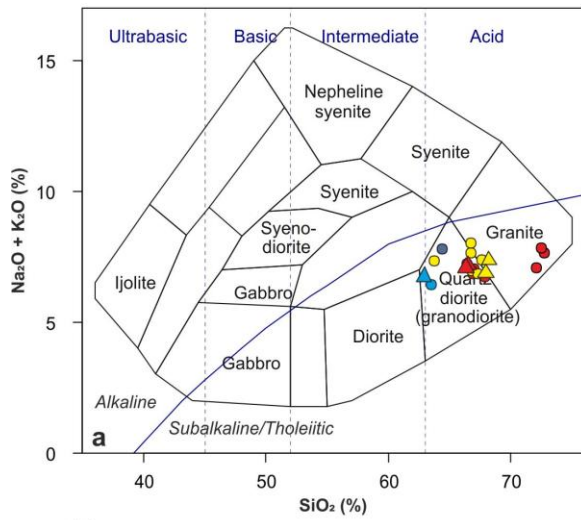


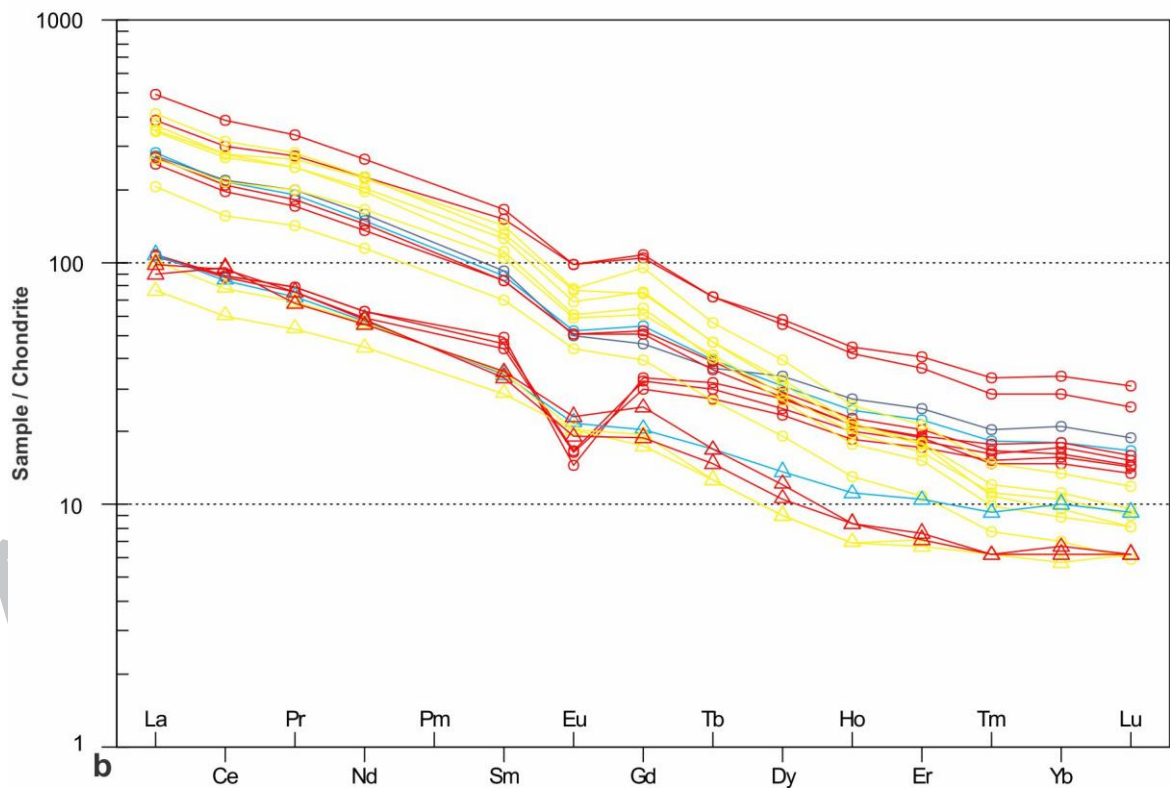
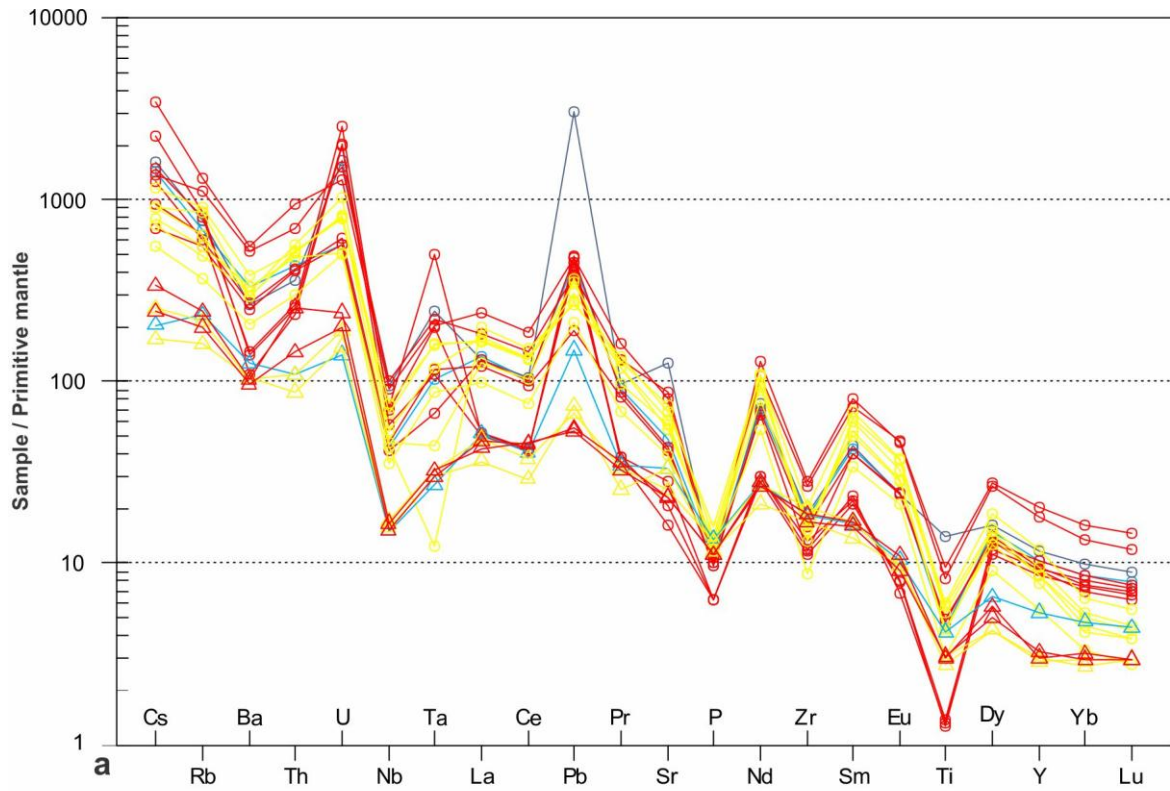


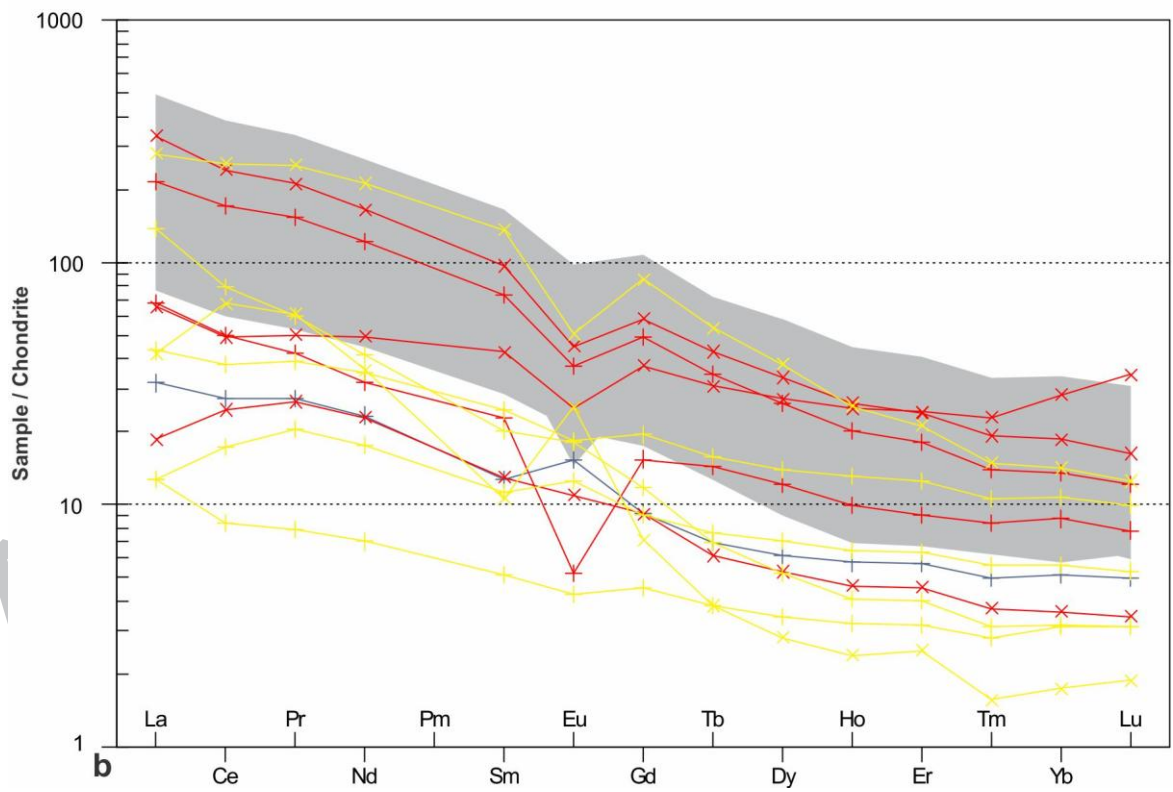
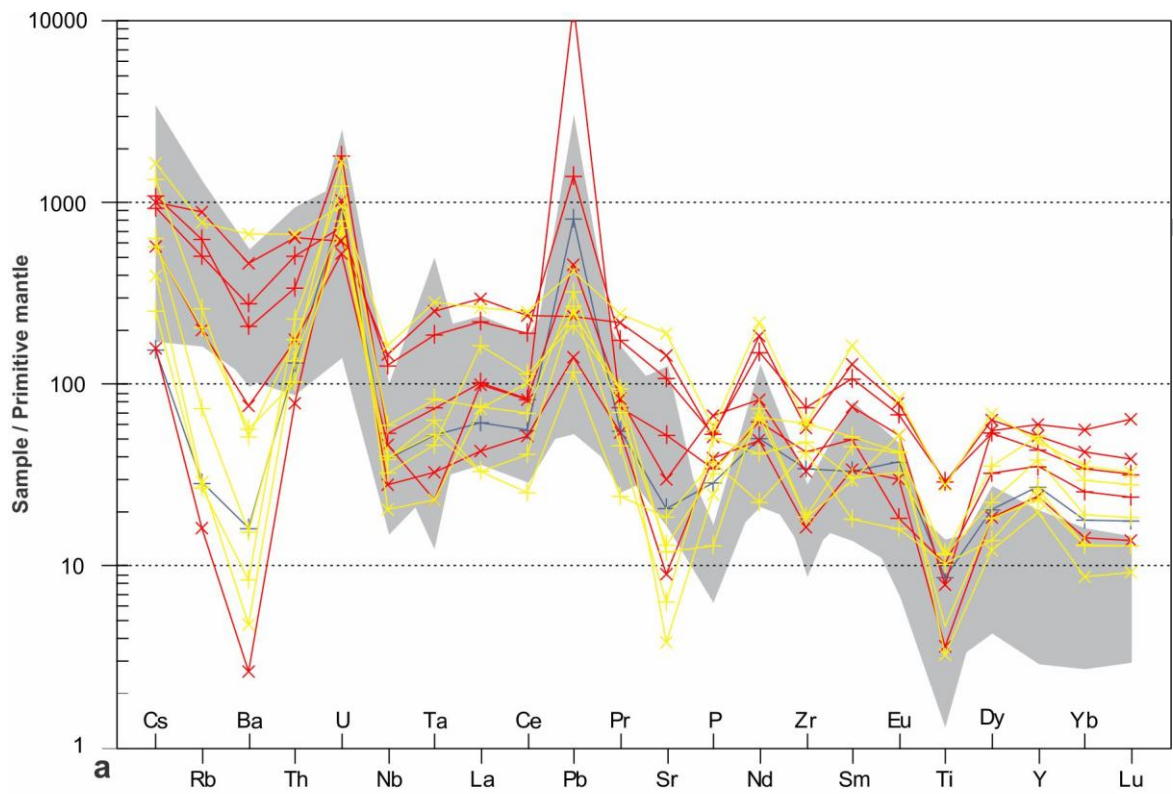


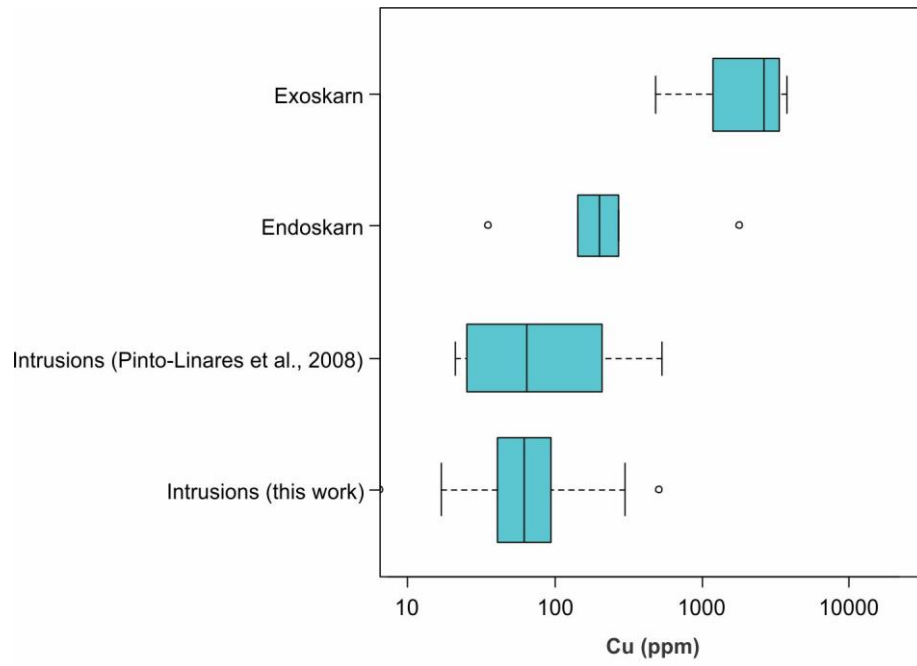


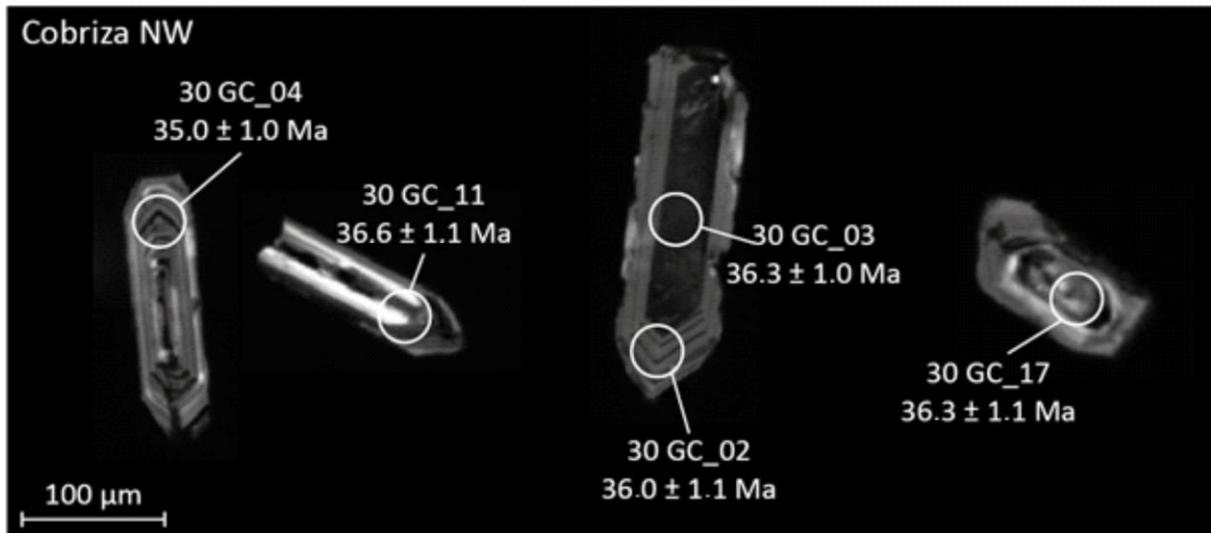




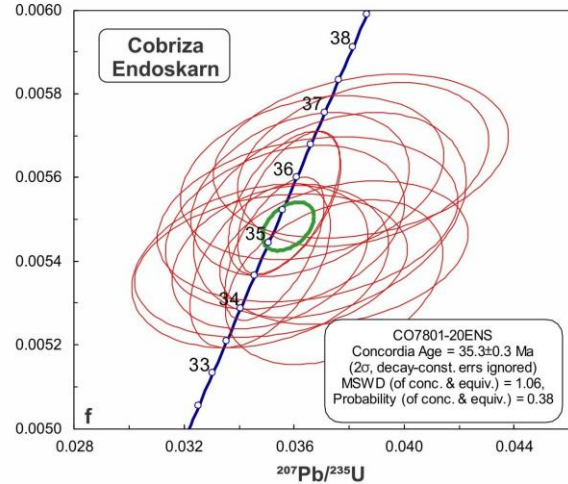
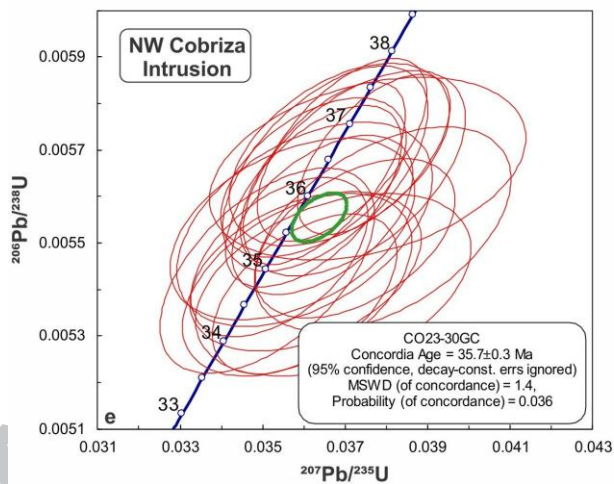
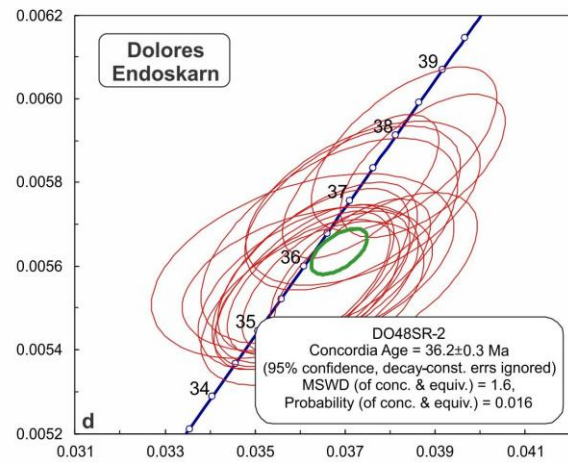
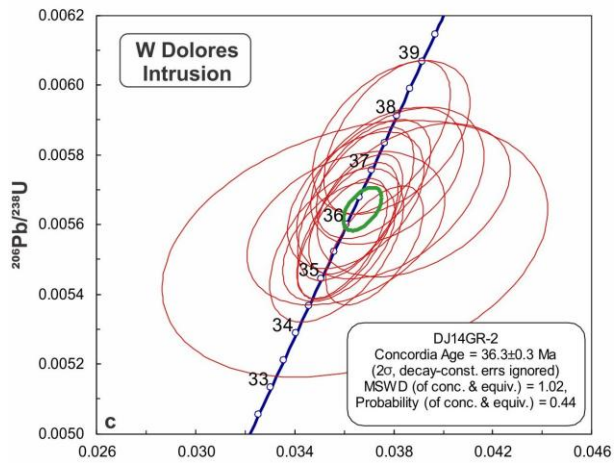
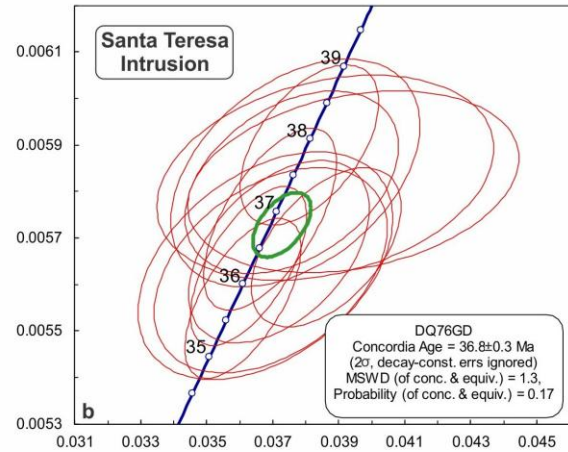
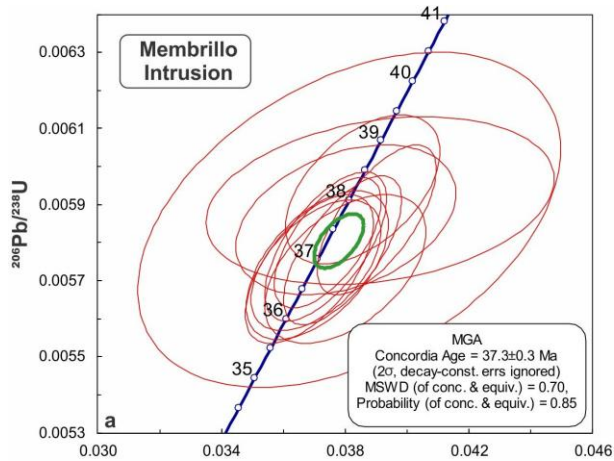


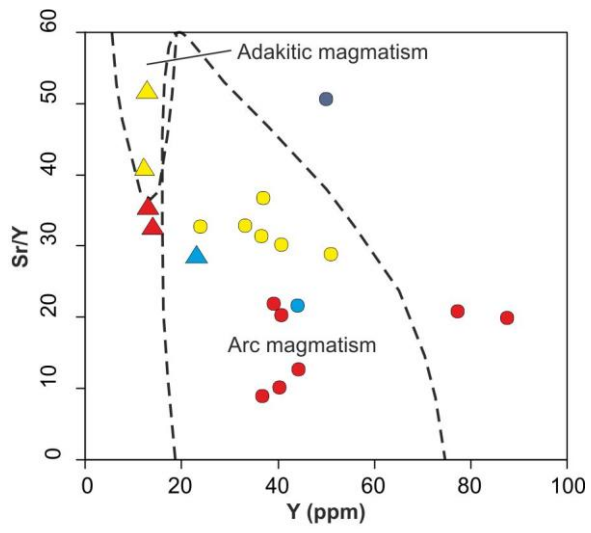




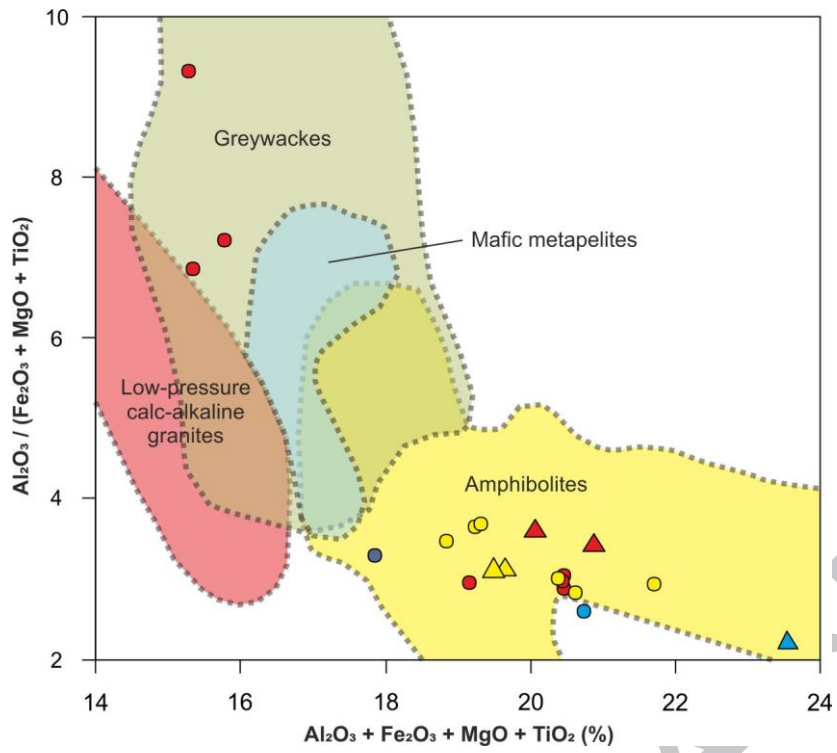


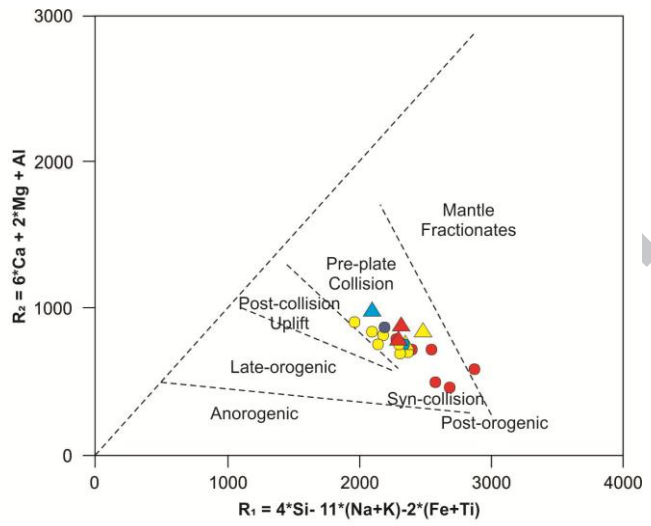
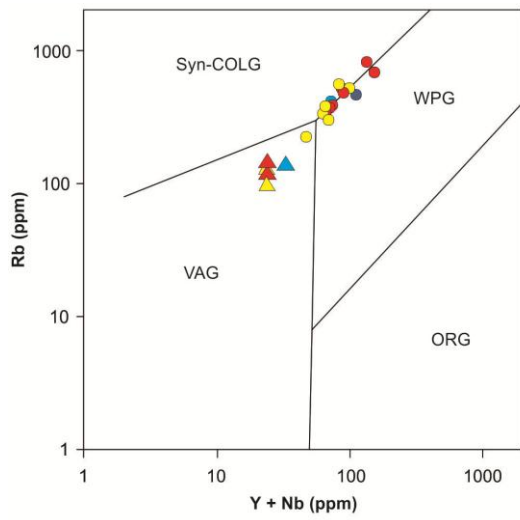
ACCEPTED MANUSCRIPT



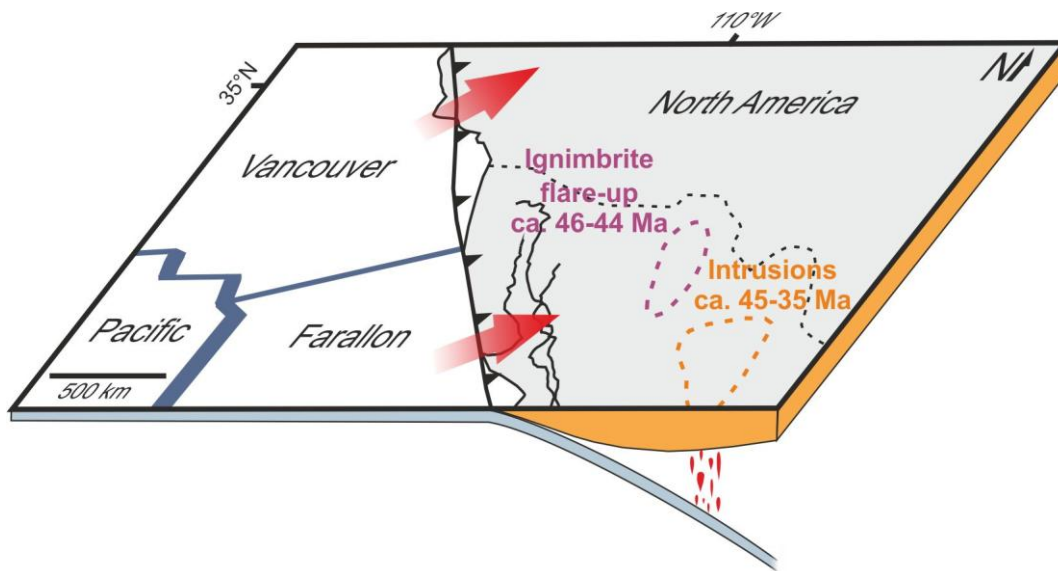


ACCEPTED MANUSCRIPT





ACCEPTED MANUSCRIPT



ACCEPTED MANUSCRIPT

ACCEPTED MANUSCRIPT

	Mem-brillo	Santa Teresa	Dolores E 1	Dolores E 2	Dolores E 3	Dolores W 1	Dolores W 2	Dolores W 3	Dolores W 4	Cobriz a NW 1	Cobriz a NW 2	Cobriz a NW 3	Cobriz a SE 1	Cobriz a SE 2	Cobriz a SE 3
	MGA	DQ-76 GD	DO-48 GM1	DO 48 GR1	DO 48 GR2	DJ-14 GM1	DJ-14 GR1	DJ-14 GR2	DJ-10 GM1	CO 2330 GR-W	CO 2330 GC	CO 2330 GR-E	CO 7820 GR-S	CO 7820 GR-N	CO 7816 GR
SiO ₂	63.47	64.39	66.95	66.97	66.44	72.74	72.12	72.49	67.91	67.62	66.72	66.77	66.82	67.33	63.75
TiO ₂	0.65	0.59	0.62	0.60	0.65	0.21	0.20	0.23	0.60	0.60	0.67	0.58	0.64	0.61	0.81
Al ₂ O ₃	14.99	13.68	15.18	15.41	15.29	13.39	13.80	13.86	14.32	15.11	15.20	14.63	15.23	15.30	16.19
Fe ₂ O ₃	3.89	2.80	3.54	3.40	3.36	1.42	0.97	1.33	3.22	2.70	2.48	2.82	3.86	3.65	3.50
MnO	0.06	0.05	0.03	0.03	0.03	0.03	0.02	0.04	0.03	0.03	0.03	0.04	0.04	0.04	0.03
MgO	1.21	0.77	1.11	1.05	1.13	0.32	0.31	0.36	1.02	0.83	0.97	0.81	0.88	0.82	1.20
CaO	3.77	5.30	3.44	3.32	4.07	1.73	2.79	1.91	3.63	3.91	4.44	3.98	3.25	3.35	4.98
Na ₂ O	2.26	1.55	2.93	2.82	2.97	2.75	2.09	3.20	2.52	3.31	3.22	2.86	3.28	3.34	3.75
K ₂ O	4.17	6.25	3.92	4.21	4.24	4.90	4.98	4.62	4.21	4.05	4.44	5.17	3.69	3.52	3.60
P ₂ O ₅	0.22	0.20	0.21	0.21	0.22	0.13	0.13	0.13	0.20	0.25	0.29	0.24	0.27	0.25	0.33
H ₂ O	2.18	1.20	1.22	1.17	0.84	1.20	1.13	0.90	1.03	0.84	0.74	0.95	1.18	1.08	0.99
CO ₂	2.22	2.35	0.28	0.32	0.17	0.77	0.74	0.42	0.57	0.30	0.33	0.67	0.37	0.32	0.23
Li	79.54	61.85	41.31	97.96	78.15	47.61	27.87	33.38	44.12	67.62	58.32	54.50	71.98	65.39	53.69
Sc	13.08	74.60	11.58	20.29	24.60	4.02	5.29	6.05	10.65	6.45	10.55	8.24	6.06	5.06	11.39
Ti	5226.69	16942.39	5749.50	9846.83	11504.54	1514.72	1602.47	1645.11	5874.61	5079.77	7290.49	6958.94	5198.78	3708.66	6406.25
V	75.51	209.35	66.73	144.56	189.90	26.87	35.40	22.63	61.38	67.52	114.46	66.30	41.42	34.12	86.29
Co	9.75	15.33	7.22	11.96	13.90	1.78	1.23	1.68	7.32	5.03	6.51	6.70	6.11	4.45	7.46
Ni	5.33	5.90	4.32	7.90	10.26	1.50	2.16	1.51	4.46	4.49	6.01	6.57	3.45	2.55	5.60
Cu	23.78	520.44	66.59	61.72	96.39	74.49	127.46	53.76	300.30	16.85	49.94	91.44	33.61	6.51	60.55
Zn	82.93	n.b.	63.22	105.92	126.64	34.21	53.36	270.19	191.93	80.27	82.42	92.62	85.97	69.64	64.93
Y	44.09	49.96	40.71	77.23	87.56	36.66	44.30	40.35	39.05	36.61	50.97	40.58	33.16	23.78	36.98
Zr	189.79	197.27	122.29	295.58	276.17	118.22	123.92	139.90	166.20	169.80	215.04	160.09	170.69	92.61	137.93
Nb	28.82	63.02	30.70	60.21	65.73	37.89	45.53	47.43	27.17	30.64	49.48	43.73	34.91	23.44	28.50
Mo	8.62	113.02	17.14	11.28	29.08	70.72	25.87	9.93	61.69	10.29	22.60	57.70	2.34	1.75	4.17
Cd	0.90	5.61	0.40	0.63	0.66	0.78	2.23	11.48	5.80	0.88	1.00	1.23	0.18	0.15	0.48
Sn	17.32	227.49	21.64	47.46	39.64	15.06	22.67	26.62	31.15	8.42	17.64	50.24	5.52	5.03	15.09
Sb	4.38	30.71	1.06	3.36	3.01	2.40	4.43	3.70	2.24	0.75	0.94	1.32	0.23	0.15	0.27
Rb	412.71	458.02	362.50	793.67	668.57	386.18	483.21	507.74	332.63	381.96	510.89	549.01	297.17	219.72	334.66
Sr	953.32	2531.85	823.11	1606.51	1746.54	325.15	561.21	409.68	856.42	1147.06	1468.71	1224.31	1091.07	779.56	1360.42
Cs	30.25	33.87	26.65	72.11	28.77	19.74	31.14	46.97	14.49	19.16	19.22	24.53	15.09	11.67	16.36
Ba	2171.81	1745.72	1772.40	3690.36	3410.91	717.31	972.59	932.25	1645.02	1917.29	1930.95	2532.47	2061.30	1370.49	2211.27
La	88.25	85.74	78.83	154.09	118.99	32.68	33.53	33.37	84.54	82.41	108.71	107.21	114.88	63.57	127.71
Ce	174.15	176.05	157.95	311.17	245.65	69.59	71.45	70.99	167.91	173.30	227.17	219.45	224.81	126.09	253.71
Pr	23.32	24.41	20.91	41.20	33.51	9.25	9.70	9.67	22.30	24.42	32.55	30.24	30.33	17.23	34.70
Nd	89.43	94.91	81.72	160.47	134.86	35.50	37.86	37.37	85.84	99.11	132.93	120.80	116.79	68.12	135.85
Sm	17.22	17.98	16.29	32.42	29.58	8.57	9.61	9.02	16.39	20.46	27.75	24.26	21.47	13.64	25.45
Eu	3.80	3.68	3.70	7.16	7.24	1.21	1.06	1.23	3.73	4.33	5.74	5.05	4.44	3.25	5.62
Gd	14.12	11.91	13.53	26.84	27.67	7.77	8.57	8.34	13.08	15.84	24.52	19.40	16.71	10.23	19.25
Tb	1.88	1.74	1.83	3.39	3.42	1.30	1.50	1.41	1.70	1.96	2.67	2.21	1.90	1.28	2.22
Dy	9.97	10.85	9.41	17.75	18.78	7.52	8.72	8.04	8.93	9.24	12.70	10.50	8.60	6.15	10.09
Ho	1.76	1.97	1.62	3.01	3.23	1.34	1.54	1.43	1.52	1.41	1.85	1.56	1.28	0.93	1.51
Er	4.70	5.21	4.30	7.71	8.56	3.59	4.03	3.83	3.93	3.47	4.45	3.76	3.17	2.27	3.71
Tm	0.59	0.66	0.54	0.92	1.08	0.49	0.57	0.52	0.48	0.36	0.48	0.39	0.32	0.25	0.35
Yb	3.77	4.38	3.36	5.93	7.11	3.29	3.75	3.59	3.06	2.21	2.82	2.35	1.86	1.46	1.99
Lu	0.54	0.61	0.47	0.81	0.99	0.46	0.51	0.49	0.43	0.29	0.38	0.31	0.26	0.19	0.26
Hf	9.32	7.84	6.36	15.88	13.55	7.83	8.87	9.07	8.20	8.46	10.44	8.59	8.89	5.01	6.63
Ta	3.78	8.96	4.35	7.44	8.22	4.06	7.35	18.46	2.47	1.65	5.87	6.03	4.41	3.24	0.46
W	11.05	40.89	4.22	44.41	36.14	9.63	174.94	33.92	18.42	4.86	8.10	16.35	2.06	2.57	2.72
Tl	7.00	14.98	2.43	5.58	3.42	2.77	3.53	3.86	2.28	2.26	2.57	3.37	1.86	1.37	2.18
Pb	68.39	459.56	28.32	72.26	57.89	74.09	62.67	68.15	72.49	55.47	45.82	52.67	41.13	31.90	39.38
Bi	1.50	31.10	5.00	0.96	4.77	5.45	19.31	2.41	3.23	0.25	0.94	18.18	0.71	0.18	0.19
Th	34.46	28.86	33.09	75.70	55.25	18.68	21.28	20.36	32.62	40.58	41.49	41.45	45.21	24.09	38.72
U	11.40	32.96	12.17	25.74	30.50	39.39	50.77	40.55	11.33	16.28	15.91	15.82	20.59	9.98	10.18

La_N/Yb_N	15.78	13.20	15.82	17.52	11.28	6.70	6.03	6.27	18.63	25.14	25.99	30.76	41.64	29.36	43.27
$\text{Eu}_N/\text{Eu}_N^*$	0.75	0.77	0.76	0.74	0.77	0.45	0.36	0.43	0.78	0.74	0.67	0.71	0.72	0.84	0.78

ACCEPTED MANUSCRIPT

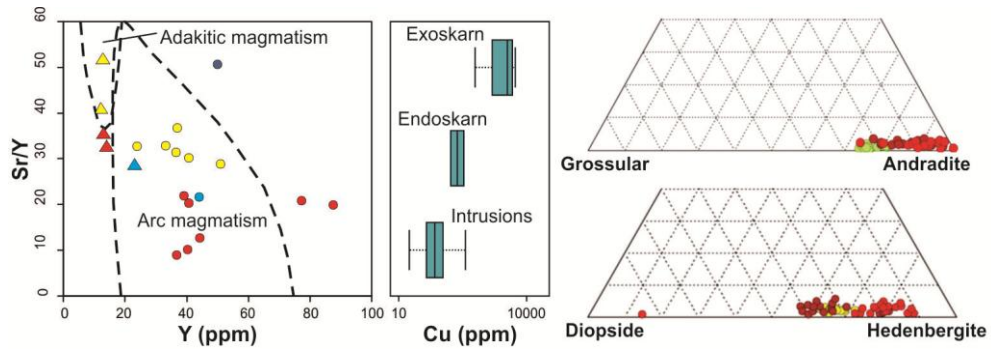
	Santa Teresa Exoskarn	Dolores E Endoskarn	Dolores E Endoskarn	Dolores W Exoskarn	Dolores W Exoskarn	Dolores W Endoskarn	Cobrizo NW Exoskarn	Cobrizo NW Exoskarn	Cobrizo NW Exoskarn	Cobrizo SE Endoskarn	Cobrizo SE Exoskarn	Cobrizo SE Endoskarn
	DQ-51 SK	DO-48 SR1	DO-48 SR2	DJ-14 SR2	DJ-10 SR2	DJ-10 SR1	CO 2330 SL	CO 2330 SG-W	CO 2330 SG-E	CO 7820 ES	CO 7820 SG-E	CO 7816 SG
SiO ₂	42.10	46.18	58.09	67.59	55.54	48.41	36.82	37.42	41.60	55.51	40.56	36.10
TiO ₂	0.12	0.05	0.69	0.16	0.73	0.03	0.16	0.19	0.15	0.69	0.06	0.03
Al ₂ O ₃	3.23	4.82	17.61	11.42	14.67	0.60	2.85	4.19	3.79	18.70	3.97	1.61
Fe ₂ O ₃	14.34	16.78	3.16	4.89	8.60	24.35	29.16	24.80	15.30	3.54	22.71	28.49
MnO	0.15	0.52	0.06	0.05	0.12	0.30	0.44	0.13	0.12	0.12	0.22	0.08
MgO	0.80	3.81	1.15	0.38	1.29	0.59	0.71	0.35	0.63	0.96	1.62	0.43
CaO	34.71	25.38	6.87	7.20	11.33	23.46	15.80	31.14	36.19	10.13	27.16	32.03
Na ₂ O	<0.01	<0.01	2.07	0.44	1.34	<0.01	<0.01	<0.01	<0.01	2.41	<0.01	<0.01
K ₂ O	0.04	0.30	7.63	4.10	2.95	0.01	1.40	0.19	0.01	5.54	1.10	0.02
P ₂ O ₅	0.10	0.36	0.24	0.13	0.25	0.16	0.15	0.23	0.12	0.29	0.03	0.08
H ₂ O	0.82	0.66	1.01	1.62	1.60	0.43	1.78	0.67	0.45	1.18	0.69	0.49
CO ₂	2.78	1.00	0.96	0.99	0.98	0.86	3.09	0.38	0.95	0.28	1.18	0.72
Li	6.40	38.36	18.09	36.17	39.70	9.65	28.64	6.90	3.78	95.31	11.88	5.50
Sc	4.90	3.80	14.77	5.84	12.76	1.91	5.61	7.43	6.74	7.59	1.17	1.46
Ti	963.19	842.79	5833.77	1269.47	5998.58	259.95	1250.61	1456.85	1510.68	5533.29	381.37	223.75
V	293.98	656.72	75.68	51.92	70.41	126.02	217.85	285.38	715.09	51.51	91.98	42.11
Co	6.94	42.40	5.52	5.88	16.17	16.70	51.78	7.81	5.07	10.21	13.96	3.40
Ni	50.21	79.78	8.72	11.14	12.16	21.11	95.61	29.67	55.13	9.62	23.28	22.30
Cu	489.96	142.53	270.74	3816.85	873.45	201.85	34528.83	2640.09	1617.99	35.59	2997.72	1806.54
Zn	110.69	339.95	68.52	2849.44	371.03	81.03	1234.57	136.19	51.36	181.35	136.34	26.47
Y	19.60	63.31	50.39	28.42	39.66	16.22	18.72	32.04	50.39	45.98	15.18	11.84
Zr	66.60	63.43	143.81	92.10	213.00	22.07	91.40	109.36	156.08	157.89	26.82	26.44
Nb	5.00	6.53	36.51	8.15	29.96	3.09	5.00	5.14	9.50	43.04	3.83	1.92
Mo	6.49	8.41	47.29	62.86	55.16	227.13	10.89	3.61	11.18	24.57	2.29	5.57
Cd	6.75	2.17	1.05	149.77	13.70	1.18	47.59	20.63	20.85	0.94	18.47	28.31
Sn	1018.56	696.88	126.87	502.08	153.78	322.59	1367.33	1504.62	1442.69	37.09	1515.35	2753.16
Sb	22.82	9.02	2.78	966.77	16.22	0.83	9.70	0.73	6.89	0.46	0.66	0.81
Rb	2.96	52.43	497.09	294.19	214.07	1.22	79.09	11.93	2.65	405.39	55.14	3.05
Sr	59.25	102.84	1077.99	238.91	698.32	17.12	50.23	10.00	29.08	1654.74	25.75	4.63
Cs	1.27	9.00	21.07	23.45	19.12	1.31	32.52	10.48	2.67	43.66	8.90	5.18
Ba	13.42	137.50	2085.33	606.53	936.95	0.89	76.32	12.62	5.01	3604.44	88.83	2.16
La	9.79	20.31	102.89	20.95	66.97	5.74	3.90	3.91	13.33	87.10	42.45	12.97
Ce	22.06	39.58	193.79	40.35	138.00	19.80	6.71	13.94	30.55	206.97	63.81	54.31
Pr	3.32	6.11	25.76	5.11	18.57	3.23	0.96	2.47	4.72	30.68	7.26	7.43
Nd	13.91	29.47	98.51	19.13	72.57	13.66	4.19	10.47	21.05	126.98	24.88	21.48
Sm	2.46	8.28	18.81	4.45	14.31	2.51	0.99	2.17	4.74	26.58	3.93	2.06
Eu	1.12	1.84	3.30	0.38	2.74	0.80	0.31	0.91	1.35	3.71	1.33	1.85
Gd	2.36	9.67	15.12	3.96	12.64	2.35	1.17	2.34	5.00	21.98	3.02	1.84
Tb	0.33	1.46	2.02	0.68	1.63	0.29	0.18	0.36	0.74	2.53	0.33	0.18
Dy	1.98	8.73	10.73	3.90	8.41	1.69	1.10	2.27	4.48	12.16	1.66	0.90
Ho	0.41	1.78	1.88	0.71	1.44	0.33	0.23	0.46	0.93	1.82	0.29	0.17
Er	1.19	5.05	4.99	1.88	3.76	0.95	0.66	1.32	2.61	4.44	0.83	0.52
Tm	0.16	0.74	0.62	0.27	0.45	0.12	0.09	0.18	0.34	0.48	0.10	0.05
Yb	1.06	5.89	3.87	1.81	2.80	0.75	0.65	1.17	2.23	2.94	0.66	0.36
Lu	0.16	1.10	0.52	0.25	0.39	0.11	0.10	0.17	0.32	0.40	0.10	0.06
Hf	2.66	2.22	7.93	6.66	10.16	0.67	4.11	4.69	4.75	9.25	1.01	0.89
Ta	0.44	0.13	4.71	0.74	2.98	0.22	0.58	0.45	0.87	5.57	0.37	0.13
W	84.52	28.08	44.96	431.49	47.12	158.46	16.64	116.22	7.06	9.57	524.94	1210.29
Tl	0.11	0.81	3.17	3.40	1.86	0.05	4.28	0.99	0.13	2.53	1.05	0.24
Pb	109.76	46.22	17.11	6386.55	248.23	7.91	5.89	20.66	27.35	40.64	14.43	18.26
Bi	146.95	420.53	21.08	641.67	24.81	10.75	283.58	170.77	386.85	3.00	145.87	223.88
Th	3.62	5.70	40.57	15.74	28.88	1.77	5.95	4.04	8.68	43.43	2.65	4.34
U	17.78	7.60	9.50	48.52	12.59	20.56	14.21	11.62	27.27	18.55	12.65	43.15
La _N /Yb _N	6.23	2.32	17.92	7.80	16.13	5.16	4.05	2.25	4.03	19.97	43.36	24.29
Eu _N /Eu _N *	1.42	0.63	0.60	0.28	0.62	1.01	0.88	1.23	0.85	0.47	1.18	2.91

Sample	Spike	K ₂ O [wt.-%]	⁴⁰ Ar* [nl/g]	⁴⁰ Ar* [%]	Age [Ma]	2σ [Ma]	2σ [%]
Santa Teresa	4950	7.88	9.00	96.79	35.05	0.89	2.5
Dolores E	4948	9.13	9.18	78.13	30.92	0.41	1.3
Dolores E	4949	9.18	10.59	86.23	35.43	0.45	1.3
Dolores W	4947	8.98	10.25	87.60	35.07	0.55	1.6
Cobriza SE	4943	8.98	7.92	97.46	27.13	0.41	1.5
Cobriza SE	4941	9.33	10.26	94.55	33.80	0.36	1.1
Cobriza NW	4934	8.88	9.9	95.41	34.23	0.60	1.8
Cobriza NW	4935	8.86	9.83	97.02	34.06	0.59	1.7

Sample	Re [ppm]	2 σ [ppm]	¹⁸⁷ Os [ppb]	2 σ [ppb]	Age [Ma]
Standard 1 (ARM 2007)	11.3	0.1	3.3	0.03	27.64
Standard 2 (ARM 2007)	11.0	0.1	3.2	0.03	27.70
CO-MoS ₂ 1	39.6	0.4	15.7	0.15	37.80
CO-MoS ₂ 2	39.0	0.4	15.7	0.15	38.34
Calculated age					38.07 ± 0.27

- Geochemical and geochronological data of the Santa María de la Paz Cu-Au skarns
- Eocene intrusions emplaced in post-Laramide continental arc setting
- U-Pb and Re-Os data indicate contemporaneous magmatism and skarn mineralization
- Dominant andradite and hedenbergite compositions of skarn rocks
- Cu-Au together with Fe, Ni, Sn, Sb, Zn, W and Bi concentrated in exoskarn rocks

ACCEPTED MANUSCRIPT



ACCEPTED MANUSCRIPT